Energy Storage Materials 88 (2026) 105091

Contents lists available at ScienceDirect

Energy Storage Materials

journal homepage: www.elsevier.com/locate/ensm

Thermodynamic and kinetic insights into the sodium storage mechanism in bio-waste derived hard carbon anodes for sodium-ion batteries

Shuting Zhang [a,b], Mohsen Sotoudeh [a,b], Robert Leiter [a,b], Wenbo Wang [a,b], Lukas Pfeiffer [c], Simon Fleischmann [a,b], Peter Axmann [c], Dominic Bresser [a,b,d], Maider Zarrabeitia [a,b,e,*], Stefano Passerini [a,b,f,*]

[a] Helmholtz Institute Ulm (HIU), Helmholtzstrasse 11, 89081 Ulm, Germany
[b] Karlsruhe Institute of Technology (KIT) P.O. Box 3640, 76021 Karlsruhe, Germany
[c] Centre for Solar Energy and Hydrogen Research Baden-Württemberg (ZSW) Helmholtzstraße 8, 89081 Ulm Germany
[d] Ulm University (UUlm), 89069 Ulm, Germany
[e] Institute of Materials Science of Seville, Spanish National Research Council – University of Seville, C/Américo Vespucio 49, 41092 Seville, Spain
[f] Austrian Institute of Technology (AIT), Center for Transport Technologies, Giefinggasse 2, 1210 Wien, Austria

ARTICLE INFO

Keywords:
Hard carbon
Biowaste anode material
Na-ion storage
Sodium-ion batteries

ABSTRACT

Sodium-ion batteries (SIBs) are attractive alternatives to lithium-ion batteries owing to their comparable performance, improved safety, and reduced reliance on critical raw materials. Hard carbon (HC) is widely regarded as the most practical anode for SIBs; however, conventional HCs still suffer from limited reversible capacity, poor rate capability, and an incompletely understood Na^+ storage mechanism. Here, we investigate hazelnut shell–derived HC synthesized via a sustainable water-washing route, with a particular focus on the effects of particle size and pyrolysis temperature on electrochemical behavior. We demonstrate that smaller particle sizes improve reversible capacity and cycling stability, while uniformly distributed nanoscale inorganic impurities regulate the evolution of pore structure in HC, thereby enhancing Na^+ storage. A clear thermodynamic relationship between the sloping and plateau capacities is identified. *Operando* X-ray diffraction and ex-situ Raman spectroscopy reveal that Na^+ storage proceeds through chemisorption in the sloping region and diffusion-controlled Na clustering within pseudographitic domains in the low-voltage plateau, accompanied by reversible structural disordering. Density functional theory and molecular dynamics simulations further confirm that Na^+ preferentially chemisorbs at disordered carbon layers at higher potentials and subsequently forms semi-metallic Na clusters within nanopores adjacent to pseudographitic layers at lower potentials, closely linked to the pre-adsorbed Na^+ species. These findings provide fundamental mechanistic insight into Na^+ storage in biomass-derived HC and offer clear guidelines for optimizing HC anodes toward high-performance SIBs.

1. Introduction

In the quest for sustainable, cost-effective energy storage solutions, sodium-ion batteries (SIBs) have emerged as a promising alternative/complement to lithium-ion batteries (LIBs) [1–3]. The development of SIB technology is motivated by concerns about the limited supply and uneven distribution of lithium and other LIB elements, such as cobalt, nickel, and natural graphite [4,5]. In fact, SIBs benefit from the abundant and inexpensive sodium resources and are not dependent on critical and/or high-environmental-impacting raw materials [6]. Together with similar electrochemical properties to LIBs, these advantages make SIBs an attractive option for large-scale energy storage and lightweight electromobility, as announced by JMEV EV3 Motors Group [7–9]. However, developing efficient and durable anode materials for SIBs remains a significant challenge [10]. Conventional anode materials often fall short in terms of capacity, stability, and/or environmental sustainability, and the still-controversial mechanism of hard carbon (HC) anodes further impedes their standardization [11,12].

Various carbon precursors can be employed to manufacture HC anode materials. Traditional precursors, such as sugars and polymers [13], often require acidic or basic pre- and/or post-treatments [14], resulting in high synthetic costs, low yields (usually < 30%), and

* Corresponding authors.
E-mail addresses: maider.ipina@kit.edu (M. Zarrabeitia), stefano.passerini@kit.edu (S. Passerini).

https://doi.org/10.1016/j.ensm.2026.105091
Received 26 January 2026; Received in revised form 23 March 2026; Accepted 6 April 2026
Available online 6 April 2026

sustainability hazards, which significantly reduce the sustainability of SIBs [15]. In contrast, biowaste is underutilized and often burned in the open air, releasing CO_2, volatile organic compounds, and fine particles, thereby disrupting carbon neutrality and contributing to air pollution [16]. An optimal and sustainable use of biowaste is indeed found in energy-related applications [17], including the use of biowaste-derived HC as sustainable and efficient anode materials for SIBs, paving the way for future advancements in energy storage technology [18]. Different biowastes have been investigated as potential sources for HC anode materials, including biowaste rich in hemicellulose, lignin, and pectin [19,20]. Lignin-rich biowaste, in particular, was shown to yield HCs with high performance, including capacity and initial Coulombic efficiency (ICE), for SIBs [21]. Nonetheless, the rational design of optimal HC anode materials requires a deep understanding of their Na^+ storage mechanism. Indeed, the optimal balance between the sodiation processes, occurring in a sloping voltage region and a low voltage plateau region, as well as the processes involved in each region, remains a matter of controversy [22,23]. Other main challenges correspond to the ICE, where most HC anodes typically do not exceed 80%, which is not optimal for commercial applications [24,25]. It has been reported that increasing the pyrolysis temperature improves the ICE by reducing defects and open porosity, thereby lowering the irreversible capacity [24,26]. This indicates that the pyrolysis temperature is a critical parameter for developing industry-relevant HC anode materials, as it significantly affects electrochemical performance, with specific capacities peaking at temperatures of 1200–1600 °C [24]. Nonetheless, other synthetic parameters should also be considered, such as different pre- and post-pyrolysis treatments, which are often required to achieve optimal HC performance, but depend on the specific biowaste precursor [27].

Previous research identified hazelnut-shells, which have a high lignin content (≈48% lignin), as an excellent precursor for fabricating HC anode materials for SIBs, employing a simple water-wash pretreatment [28,29]. This method is both environmentally friendly and economically viable, as confirmed by Life Cycle and Cost Assessments [30]. However, as mentioned, this HC material still suffers from several issues, and the Na^+ storage mechanism remains unclear. Therefore, this work focuses on elucidating the Na^+ storage mechanism in sustainable hazelnut-shell-derived HC as anode material for SIBs. To date, mechanistic studies have primarily focused on structural changes during sodiation, which can be broadly divided into two regions: the high-voltage sloping region capacity (HVC) and the low-voltage plateau region capacity (LVC), around which the controversy centers. Supported by X-ray diffraction (XRD) results, some studies suggest that LVC is associated with the Na^+ intercalation process in the pseudographitic layers, leading to the formation of NaC_x compounds, similar to the low-voltage plateau observed upon Li^+ intercalation in graphite [31]. Transmission electron microscopy (TEM) studies reveal a more disordered structure after complete Na^+ insertion [32]. On the contrary, some studies suggest that simultaneous insertion and adsorption of Na^+ occur in HVC, whereas nanopore filling occurs in LVC [33–36]. *Operando* Raman spectroscopy supports this mechanism, showing a reversible decrease of the G-band peak in HVC during charging and discharging [37]. Moreover, Han *et al.* reported that the Na steady-state in HC at 0.01 V differs significantly from that at 0.03 V, leading to Na clusters [38]. This may involve the formation of two-dimensional metallic Na clusters that are close enough to share a conducting electron, as indicated by *ex-situ* atomic pair distribution function (PDF) analysis [38]. Further insights are provided by *operando* solid-state ^{23}Na nuclear magnetic resonance (ssNMR) and PDF analysis, suggesting that capacity results from Na^+ adsorbing onto pore surfaces, defects, and expanded layers before aggregating into larger quasi-metallic clusters or intercalated between expanded carbon sheets at lower voltages [39]. Vasileiadis *et al.* simulated this pore-filling mechanism using density functional theory (DFT) calculations, demonstrating that Na clusters "sandwiched" between graphene sheets have lower interface energy than isolated Na layers or clusters with exposed surfaces [40]. Despite these advancements, each study explains only part of the phenomenon, failing to establish the relationship between the different stages of the Na^+ storage process in HC. In addition, these studies investigated HC materials with varying properties, further confirming that extrapolating results from a specific HC to all HCs is, in general, not accurate.

Therefore, this study explores the use of biowaste materials as a cost-effective and sustainable approach to developing HC anodes for SIBs, focusing on hazelnut shell biowaste, a readily available and renewable resource in Europe. The use of biowaste not only addresses environmental concerns by recycling waste, but also offers economic benefits [41,42]. Despite previous research, the role of impurities and the detailed mechanisms of Na^+ storage remain unclear. Hence, this work aims to fill these gaps by thoroughly investigating the structure and composition of hazelnut shell-derived HC and proposing a novel explanation for the Na^+ storage mechanism, distinguishing between the HVC and LVC regions, based on both experimental and theoretical studies, demonstrating their interrelated nature and their impact on the overall battery performance.

2. Experimental section

2.1. Materials preparation

Hazelnut shells were initially washed with deionized (D.I.) water and subsequently dried in an oven at 80 °C until dehydration. The dried hazelnut shells were then ground in a two-step process before pyrolysis. In the first step, the shells were ground into particles smaller than 1 mm using a mechanical mill (IKA®, sieve: MF10.1). In the second step, the material was further ground in a rotor mill (Retsch ZM 300) using a 0.08 mm sieve. The resulting powder was sieved to micrometer-sized fractions using a sieve shaker (Retsch AS 200) to obtain fine powders of different particle sizes. The resulting fine powders were categorized into three size fractions: 100–50 μm, 32–25 μm and < 25 μm. The HC powder fractions 100–50 μm (labeled as 1100–100) and 32–25 μm (labeled as 1100–32) were pyrolyzed in a tubular furnace (Nabertherm, P330) at 1100 °C for 1 h (heating rate of 1 °C min^{-1}) under Ar atmosphere. For the powder fraction with particles < 25 μm, pyrolysis was conducted at 900 °C (900–25), 1000 °C (1000–25), 1100 °C (1100–25) and 1200 °C (1200–25) for 1 h (heating rate of 1 °C min^{-1}) under argon atmosphere. Finally, the HCs with different particle sizes pyrolyzed at 1100 °C (labeled as S-HCs) and the HCs with particle size below 25 μm pyrolyzed at various temperatures (labeled as T-HCs), were hand-ground with a mortar and stored in a dry room (dew point below −70 °C) to prevent moisture absorption.

2.2. Materials characterization

The morphology and particle size of S-HCs were examined using high-resolution scanning electron microscopy (FE-SEM, ZEISS Crossbeam 340) with an acceleration voltage of 3 kV. Elemental analysis was conducted using Energy-Dispersive X-ray spectroscopy (EDX, Aztec, Oxford Instruments) at an accelerating voltage of 10 kV. The particle size distribution of S-HCs was determined by the Mastersizer 3000+ particle size analyzer. For hazelnut shells with particle size < 25 μm, pyrolysis at temperatures up to 1200 °C was analyzed using thermogravimetric analysis coupled with mass spectrometry (TGA-MS). Measurements were carried out in Al_2O_3 crucibles under Ar atmosphere with a heating rate of 10 K min^{-1}, using a TGA-DSC device (Netzsch STA 449 C) coupled to a mass spectrometer (Netzsch QMS 403). Microstructural properties were investigated using powder XRD and Raman spectroscopy. XRD data were recorded on a Bruker Advance D8 diffractometer with Cu Kα radiation (λ = 1.5406 Å, 1.5444 Å) in the 2θ range of 10–90°. *Operando* XRD measurements were performed in the 2θ range of 10–50°. The *operando* half-cell was assembled using 1000–25 HC as the active material, comprising 90 wt.% active material and 10 wt.% binder, without any conductive carbon. Raman spectra of the HC powders and

electrodes were collected using a confocal Raman microspectrometer (Renishaw) equipped with a 633 nm red laser and a 50 × objective lens in a back-scattering configuration. Raman spectra of each HC sample were collected at least three times (ten measurements per samples) in the range of 700–2000 cm^{-1}, using five accumulations of 10 s each. The spectra were processed for background removal and normalization using LabSpec5 software, and further deconvoluted by Gaussian-Lorentzian functions. High-resolution transmission electron microscopy (HRTEM) was used to observe the HCs pyrolyzed at different temperatures (T-HCs). HRTEM analyses were conducted using a ThermoFisher Talos F200i microscope, operated at 200 kV. TEM samples were prepared by dispersing the HC powder on Cu TEM grids coated with a holey carbon support film. The surface chemistry of the HCs was evaluated using X-ray photoelectron spectroscopy (XPS, SPECS) in fixed transmission mode, equipped with a monochromatic Al X-ray source (Al Kα, $h\nu$ = 1486.6 eV) and a PHOIBOS 150 hemispherical energy analyzer with a 2D delay line detector. The C 1 s spectra were calibrated using the graphitic peak (C = C, sp^2) at 284.4 eV as a reference and fitted with a nonlinear Shirley-type background and a 70:30 Gaussian-Lorentzian profile using CasaXPS software [43]. The porosity and specific surface area (SSA) of the HCs were determined from simulated adsorption isotherms of Ar at 87 K and CO_2 at 273 K, using a Quantachrome Autosorb-iQ-MP/XR analyzer. Prior to adsorption, the HCs were degassed at 200 °C for 15 h. Pore size distribution (PSD) was calculated using the DFT method, considering the Ar87K on Carbon Slit Pore model. The small angel X-ray scattering (SAXS) patterns were collected using a Xeuss 3.0 equipped with an Eiger2 R detector. The sample-to-detector distance was set to 100 and 1100 mm. A Cu Kα source was exploited with a beam size of 0.35 × 0.35 mm^2, obtaining a flux of ~10^7 photons s^{-1}. The instrument's sample chamber was kept under vacuum (P = 0.1 mbar) during the experiment. Each sample was exposed for 150 s. The empty capillary background was also collected and subtracted from the total scattering curve. Data treatment was performed with the Xsact software from Xenocs.

2.3. Electrode preparation and electrochemical characterization

Electrodes were prepared by mixing 80 wt.% hazelnut shell-derived HC, 10 wt.% conductive carbon (Super C45, IMERYS), 4 wt.% sodium carboxymethyl cellulose binder (Na-CMC, Sigma-Aldrich), and 6 wt.% styrene-butadiene rubber (SBR, ZEON). Na-CMC was added as a 2.5 wt.% aqueous solution in D.I. water. The mixture was homogenized using a centrifugal mixer (ARE250, THINKY) at 2000 rpm. The slurry was then cast onto a 15 μm-thick battery-grade Al foil (Wellcos Corporation), setting a wet thickness of 200 μm. The coating was dried overnight at 80 °C under ambient conditions. Disk electrodes (Φ = 12 mm) were punched and further dried under vacuum in a Büchi at 120 °C for 20 h. The average mass loading of HC electrodes was 3.5 mg cm^{-2}. Electrochemical tests were conducted in three-electrode Swagelok® T-type cells, assembled in an Ar-filled glovebox (MBraun, H_2O and O_2 < 0.1 ppm), using Na metal (99.8%, Across Organics) as both counter and reference electrodes and HCs as the working electrode. The electrolyte (240 μL) consisted of 1 M sodium hexafluorophosphate ($NaPF_6$, battery grade, Fluorochem) dissolved in a 1:1 vol. ratio of ethylene carbonate (EC, battery grade, UBE) and propylene carbonate (PC, battery grade, UBE), soaked in a glass fiber separator (GF/D, Whatman). Cyclic voltammetry (CV) tests of HCs were performed at a scan rate of 0.1 mV s^{-1} within a potential range of 0.02–2.0 V vs. Na^+/Na for 4 cycles. For T-HCs, CV tests were also conducted at scan rates of 0.05, 0.1, 0.2, 0.5, and 1 mV s^{-1}. Galvanostatic cycling and C-rate capability tests were conducted using a battery tester (Series 4000, MACCOR) within the same potential range (0.02–2.0 V vs. Na^+/Na). The specific current of 200 mA g^{-1} was defined as a 1C. All electrochemical tests were performed on cells stored in climatic chambers at 20 °C ± 2 °C. Electrochemical impedance spectroscopy (EIS) measurements were performed along CV measurements at a scan rate of 0.05 mV s^{-1}, over a frequency range of 1000 kHz to 3 mHz. Each EIS measurement required approximately 5 h. Distribution of relaxation times (DRT) analysis was carried out using DRTtools [44], based on impedance spectra collected with a multi-channel potentiostat-galvanostat (VMP3, Bio-Logic Science Instruments) at RT. For full coin cell assembly, HC electrodes (90:5:2:3 – HC:Super C45:Na-CMC:SBR composition), and a commercial $Na_3V_2(PO_4)_2F_3$ (NVPF) cathode from Tiamat (90 wt.% active material, 5 wt.% conductive carbon (Super C65), and 5 wt.% binder (PVDF)) were used in the N/P ratio of 1.3. The full cells were cycled in the 4.3–2.0 V operation voltage at 0.1C, and 1C (considering NVPF theoretical capacity).

2.4. Computational methods

DFT [45,46] calculations were performed using the Vienna Ab-initio Simulation Package (VASP) with the projector-augmented-wave (PAW) method [47,48]. Exchange–correlation effects were treated with the PBE functional [49], including long-range van der Waals interactions via the DFT-D3 scheme with Becke–Johnson damping [50]. A plane-wave cutoff of 520 eV was used for static calculations, with electronic convergence of 10^{-5} eV. Structural relaxations employed the conjugate-gradient algorithm, while lattice parameters were fixed. Spin polarization was included with initial moments of 0.6 μB per atom, Gaussian smearing was applied, and non-spherical contributions inside PAW spheres were considered. Brillouin-zone integration was performed at the Γ-point [51]. HC structures were generated via molecular dynamics using LAMMPS [52]. Initial configurations were prepared with Packmol [53] by randomly distributing 144 carbon atoms within a 12 × 12 × 12 $Å^3$ and 13 × 13 × 13 $Å^3$ periodic simulation boxes, corresponding to two different carbon densities, while ensuring no atomic overlap. The Environment-Dependent Interatomic Potential (EDIP) [54] as implemented in OpenKIM was employed to accurately capture both sp^2- and sp^3-hybridized carbon and their transformations. Simulations used a timestep of 0.5 fs under periodic boundary conditions in all directions. HC formation was modeled through a five-stage melt–quench protocol: (1) initial relaxation and short NVT equilibration at 300 K for 5 ps, (2) linear heating to 3000 K over 10 ps under NVT conditions, (3) high-temperature annealing at 3000 K for 250 ps to promote atomic diffusion and graphitic domain formation, (4) gradual cooling from 3000 K to 300 K under NPT conditions over 10 ps to allow volume relaxation, and (5) final NVT equilibration at 300 K for 5 ps followed by energy minimization. The resulting densified, disordered carbon network exhibits mixed sp^2/sp^3 hybridization, reflecting the structural characteristics of experimental HC. Structural features, including radial distribution functions and coordination number distributions, were analyzed to assess short- and medium-range order. The Na incorporation into the carbon matrix was simulated by randomly introducing 18 Na atoms into the 144-atom carbon structure using the Atomic Simulation Environment (ASE) Python package [55]. Atoms were placed at least 2.0 Å apart to avoid unphysical overlaps. Configurations were generated and subsequently relaxed using VASP to determine their electronic structures and energetics. Ab initio molecular dynamics (AIMD) simulations were performed in the NVT ensemble using a Nosé–Hoover thermostat with a 1 fs timestep, an energy cutoff of 450 eV, and a total of 15 ps simulation time. Spin-polarized calculations were used, with non-spherical PAW contributions and DFT-D3 dispersion. Symmetry was turned off to improve sampling, and structural snapshots were used to analyze sodium adsorption and cluster formation within the HC matrix.

3. Results

3.1. Morphology, composition, and structure of hazelnut-shell-derived hard carbons

The morphology, composition, including impurities, and structure of HCs were investigated and analyzed (see Fig. 1). The HCs with different particle sizes (i.e., 100–50 μm, 32–25 μm and <25 μm), confirmed by the

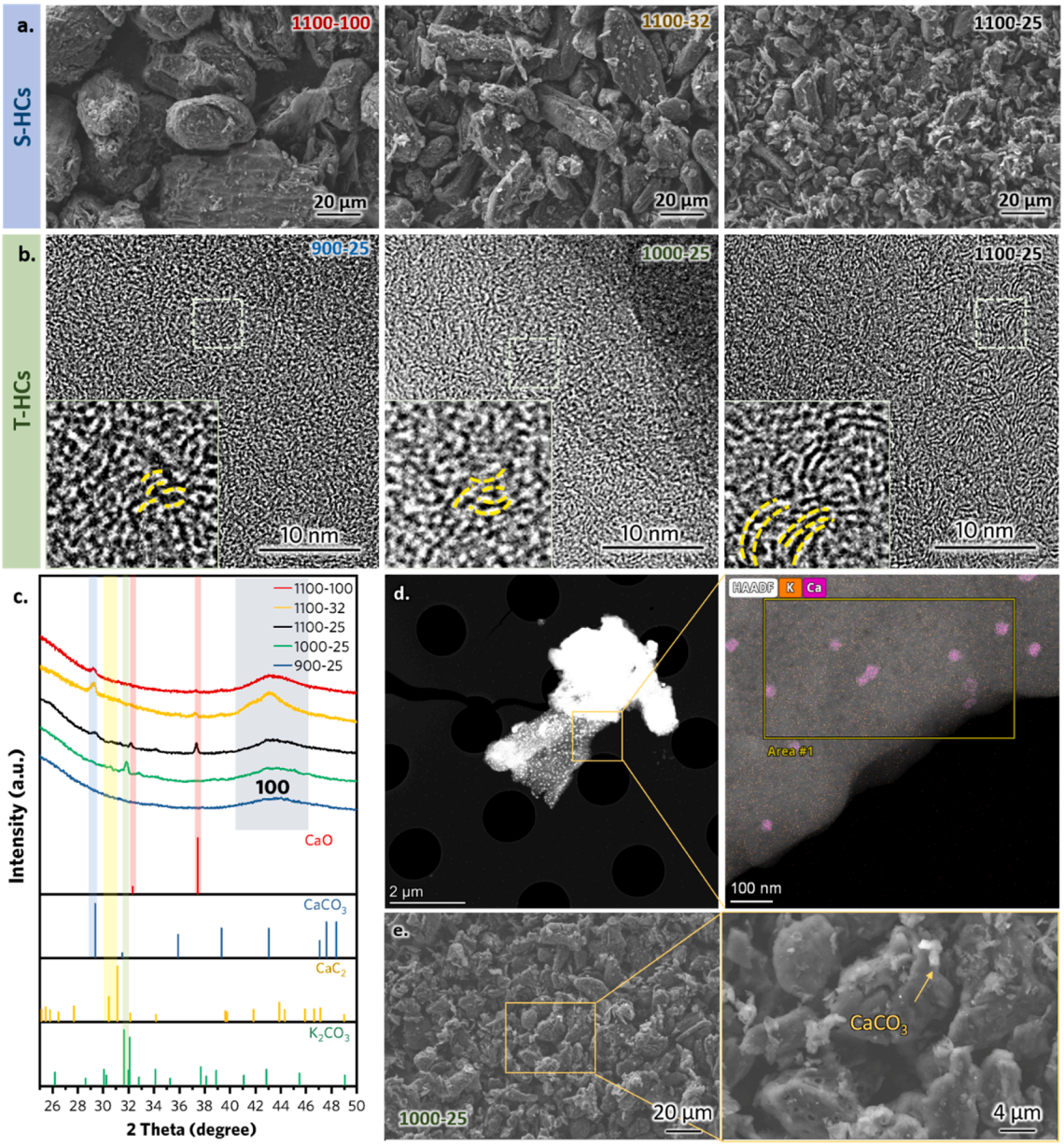

Fig. 1. Morphology, composition and structure of S-HCs and T-HCs. a. SEM images of S-HCs. **b.** HRTEM images of T-HCs. **c.** XRD patterns of S-HCs and T-HCs (also included the reference reflections of the identified impurities). **d.** High-angle annular dark-field (HAADF-STEM) image and corresponding EDX elemental mapping of the highlighted region in 1100–25 T-HC, showing the distribution of impurities (right). **e.** SEM image of 1000–25 T-HC, with the enlarged view (right) highlighting the impurity particles.

laser diffraction particle size analyzer (Fig. S1d), labeled as S-HCs, were all pyrolyzed at 1100 °C. Structural and morphological characterizations and surface chemistry analysis reveal only minor differences among the S-HC samples (Fig. S1). The SEM images of S-HCs (Fig. 1a) reveal that the particle size of the pyrolyzed carbons mostly depends on the particle size of the precursor.

To examine the effects of temperature on the pyrolysis, the precursor with the smallest particle size (< 25 µm) was subjected to different pyrolysis temperatures, such as 900 °C, 1000 °C, and 1100 °C (labeled as T-HCs). The HRTEM images in Fig. 1b reveal larger lattice-fringe domains, indicating a higher pseudographitic content in the sample pyrolyzed at elevated temperatures. These features, highlighted in the magnified images, are consistent with previous research findings [56–58]. This observation is also supported by the Raman spectroscopy

Table 1
Observed and calculated structural and pore properties of T-HCs obtained by EDX, XRD, Raman spectroscopy, and Ar and CO_2 adsorption measurements.

T-HC sample	C (at.%)	O (at.%)	K (at.%)	Ca (at.%)	R (XRD)	d_{002} (Å) (XRD)	A_D/A_G (Raman)	Ar ads. - SSA ($m^2\ g^{-1}$)	CO_2 ads. - SSA ($m^2\ g^{-1}$)
1100–25	95.3	4.0	0.4	0.3	1.91	3.83	2.66	178	140
1000–25	95.5	3.7	0.5	0.3	1.80	4.04	2.68	8	215
900–25	95.8	3.5	0.4	0.3	1.73	4.04	2.77	9	125

results (Table 1, Fig. S2), showing that the A_D/A_G ratio decreases with increasing pyrolysis temperature. Furthermore, the interlayer distance (d_{002}), calculated using Bragg's Law, is generally observed to decrease with increasing pyrolysis temperatures. The degree of structural order in the pseudographitic domains, quantified using the *R*-value based on the (002) peak in XRD patterns according to Dahn's method [59] (details in Fig. S3), also increases with temperature, confirming the TEM findings.

Impurities inherent in biowaste-derived HC materials were analyzed using XRD, XPS, TEM, and EDX. Fig. 1c shows the selected XRD patterns in the 25°−50° 2θ range, while the full patterns are provided in Fig. S3. The results indicate that higher pyrolysis temperatures lead to stronger XRD signals from impurities, suggesting that these impurities become more aggregated and crystalline at elevated temperatures. For the 1000–25 T-HC, the main crystallized impurity is K_2CO_3, whereas for the 1100–25 T-HC, the crystallized impurities are CaO and $CaCO_3$. These impurities, along with their distribution, are also evident in the EDX results (Fig. 1d). Indeed, the TEM-EDX image of the 1100–25 T-HC is in agreement with the XRD patterns and further indicates the distribution of impurities, showing the presence of CaO and $CaCO_3$, which tend to form nanoclusters during pyrolysis, whereas K_2CO_3 is more uniformly distributed. This behavior is further supported by the SEM image in Fig. 1e, which shows aggregated CaO particles on the surface of the 1000–25 HC, and by the corresponding EDX results in Fig. S4.

To further clarify the role of impurities in the Na^+ storage mechanism in T-HCs, additional TEM and EDX analyses have been performed on the pristine T-HCs and on the sodiated 1100–25 HC (Fig. 2). The pristine T-HCs in Fig. 2a show that, as pyrolysis temperature increases, impurities become more aggregated. This observation is consistent with the XRD results, which indicate that higher temperatures promote the crystallization of the inorganic impurities. The results indicate that sodiated 1100–25 HC shows regions containing aggregated CaO impurities (Fig. 2b), which achieve a much lower Na insertion (9 at.%) compared with the particles with lower impurities or uniformly dispersed nano-sized impurities (Fig. 2c), which promote a more homogeneous Na distribution and higher local Na concentration (27 at.%). The results reveal that the impurities themselves do not reduce the Na^+ insertion, but their distribution can affect it. Uniformly distributed impurities are more favorable for Na^+ storage, whereas impurity aggregation leads to the formation of larger clusters and poorer Na-storage behavior (as confirmed below).

Overall, the pyrolysis temperature is found to affect the impurity content of HCs as well as their structure and distribution, with the size and the number of pseudographitic layers increasing with temperature. The effect of impurities, however, remains unclear. Some studies suggest that impurities contribute to irreversible capacity and reduced ICE [60], while others indicate that oxide impurities can stabilize the structure and enhance durability [61].

Further correlations between the impurities and the electrochemical performance of the hazelnut-shell-derived HCs were investigated. The atomic composition (at.%) of T-HCs, as determined by surface-sensitive XPS (Table S1), reveals the opposite trend: impurity content decreases with increasing temperature. This suggests that oxygen-containing

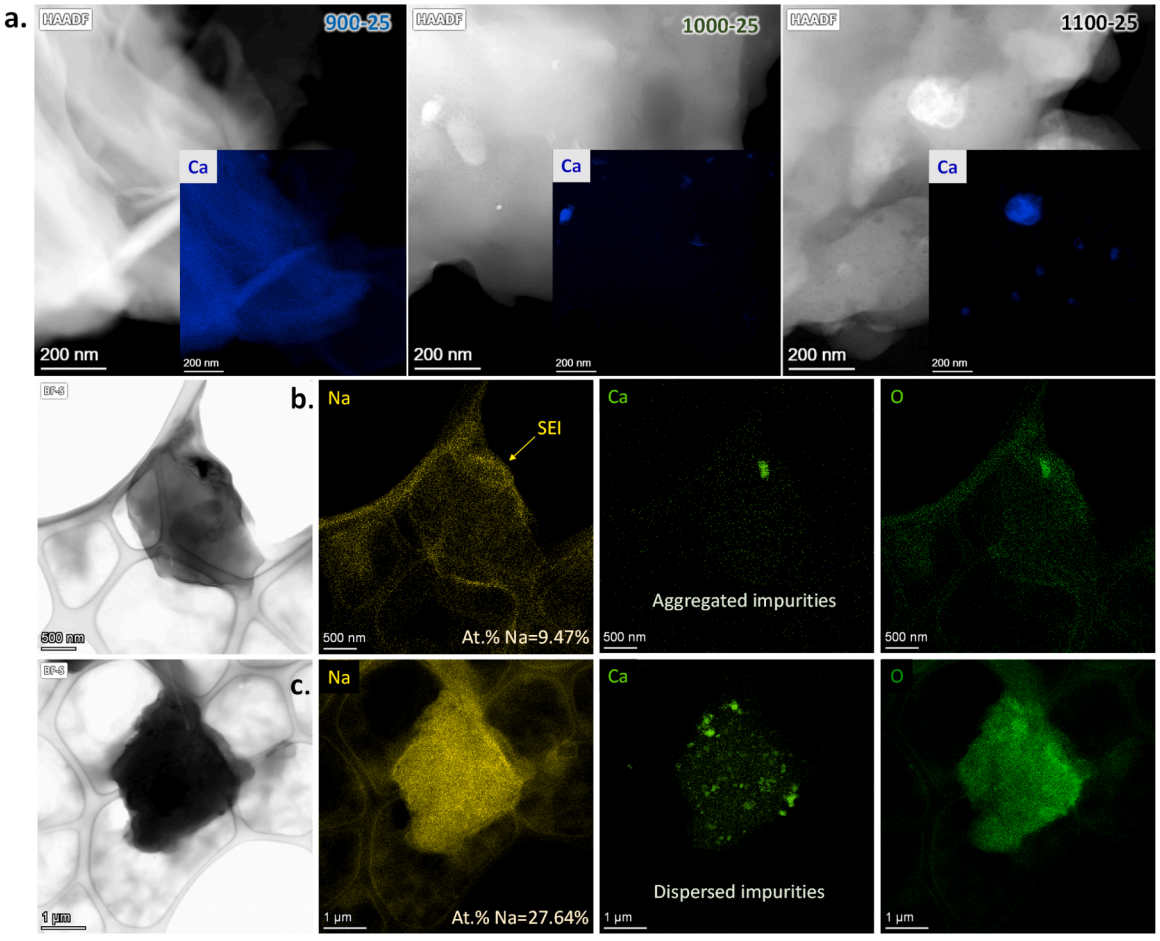

Fig. 2. TEM-EDX elemental mapping of pristine T-HCs and sodiated 1100–25 T-HC. a. HAADF-STEM images and corresponding Ca elemental maps of pristine T-HCs carbonized at different temperatures (900–25, 1000–25, and 1100–25), showing the evolution of Ca-containing impurity distribution with increasing pyrolysis temperature. TEM image and EDX elemental maps (Na, Ca, and O) of a sodiated 1100–25 T-HC region **b.** with aggregated impurities., and **c.** with more uniformly dispersed impurities.

species and potassium-rich compounds predominantly accumulate on the surface and diminish as terminal functional groups (C—O, carbonates) decompose at elevated temperatures, as shown in Fig. S2 and Table S1. In contrast, the at.% of T-HCs, as determined by EDX analysis, is summarized in Table 1. Although the carbon content is generally expected to increase with higher pyrolysis temperatures, the EDX results show similar elemental compositions across the samples. This apparent discrepancy arises because EDX probes a depth of approximately 1–3 μm, capturing only a limited portion of the surface region. The slight decrease in carbon content with increasing temperature can be attributed to the crystallization and aggregation of CaO and $CaCO_3$ impurities at higher temperatures, leading to the formation of crystalline inorganic remnants within the HC bulk. These remnants slightly enhance the detected signal from residual inorganics, consistent with the XRD patterns.

3.2. The electrochemical performance of hard carbons

Fig. 3 illustrates the electrochemical performance of hazelnut shell-derived S-HC and T-HC samples, as well as the porosimetry studies of T-HCs. The galvanostatic experimental results, including first cycle voltage profiles, capacity against cycle number, and analysis of the capacity contributions from each region (high-voltage slope and low-voltage plateau) of particle size-specific HCs (S-HCs) and temperature-specific HCs (T-HCs), are depicted in Figs. 3a-c. The first cycle voltage profiles at 0.02C, illustrated in Fig. 3a, show that the 1100–25 HC, i.e., the material with the smallest particle size, exhibits better reversibility among all S-HCs. Fig. 3b displays the proportions of HVC and LVC during the first sodiation (discharge) process, along with the corresponding ICE. Among the S-HCs, 1100–25 HC, with the smallest particle size, exhibits the best overall performance, delivering the highest capacity in the low voltage plateau region (163 mAh g^{-1}, totaling 332 mAh g^{-1}) and an ICE of 78%. Considering the similar structural characteristics among the S-HCs (see Fig. S1), the performance differences are mainly attributed to their kinetic properties due to the particle size effect.

Fig. 3c illustrates the cycling stability over 200 cycles. Among all HCs, 1000–25 HC shows the most promising long-term cycling performance, delivering 256 mAh g^{-1} after 100 cycles with a capacity retention of 94.3% (see Table 2). Once more, the S-HC materials with a larger particle size perform very poorly. However, among the small particle size T-HCs, 1100–25 HC performs worse than those carbonized at lower temperatures.

To better understand these results, CV tests were performed on all S-HCs. The first four CV cycles, presented in Figs. 3d-f, highlight 1100–25 HC as the material offering the best reversibility, in agreement with the capacity retention observed in the galvanostatic experiments. Moreover, the sharpness and intensity of its redox peaks indicate that the small particle size significantly enhances Na^+ storage properties. Its high LVC results in improved ICE due to irreversibility mainly occurring in the sloping region (note that the solid electrolyte interphase (SEI)) formation, resulting from electrolyte decomposition, occurs at 0.8 V vs. Na^+/Na) [62]. This suggests that smaller particle sizes enhance kinetic properties and extend the LVC region, thereby improving the overall electrochemical performance. Due to the excellent electrochemical

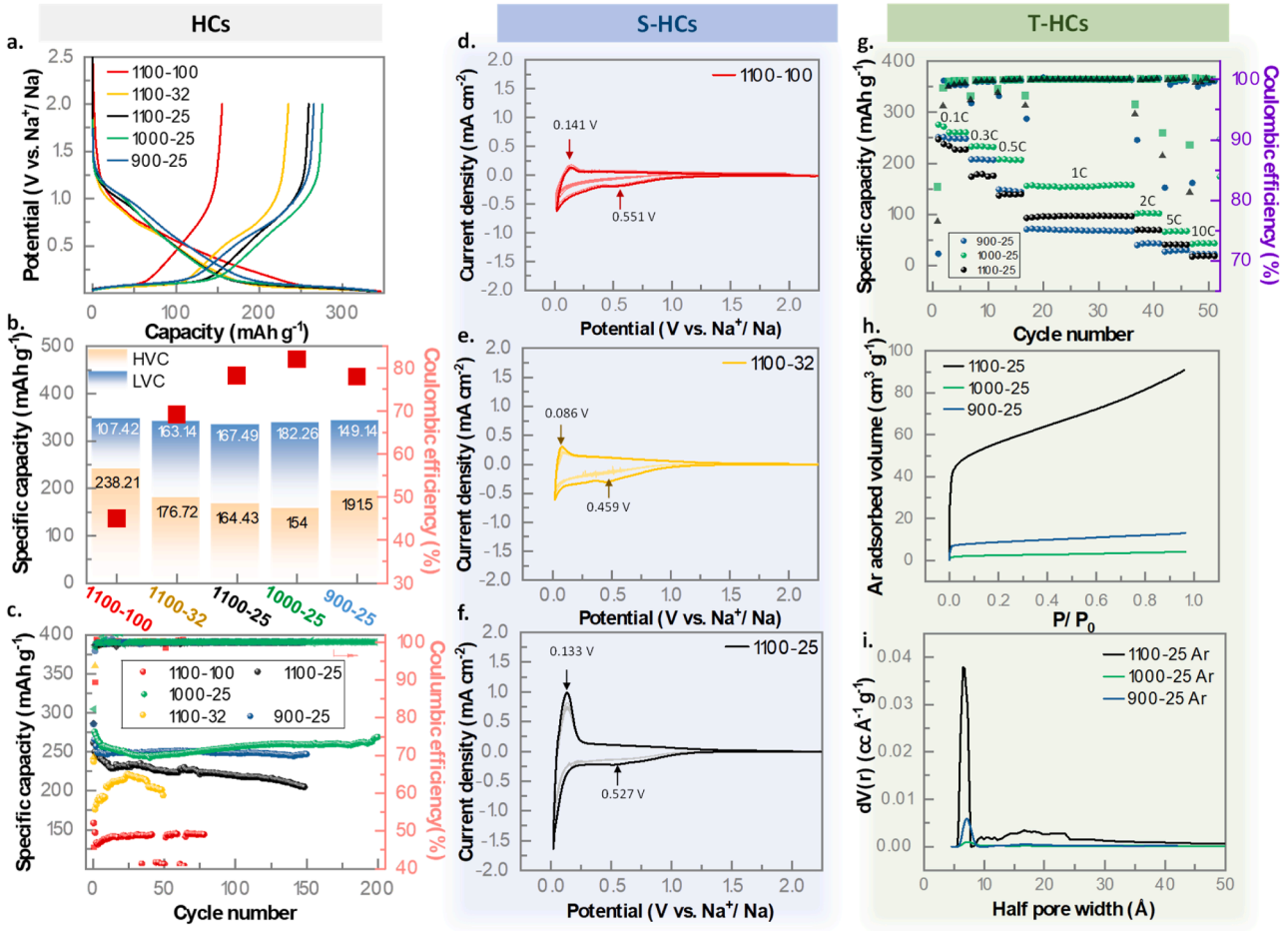

Fig. 3. Electrochemical performance analysis of S-HCs and T-HCs. a. First sodiation (discharge)/ desodiation (charge) cycle at 0.02C. **b.** Deconvolution of the HVC and LVC capacities and ICE and. **c.** Long-term cycling performance at 0.1C of all HCs. CV plots recorded during the first four cycles of **d.** 1100–100, **e.** 1100–32 and **f.** 1100–25 S-HCs. **g.** C-rate performance of T-HCs. Brunauer-Emmett-Teller (BET) measurements: **h.** Ar adsorption curves at 87 K, and **i.** Pore size distribution.

Table 2
Comparison of specific capacity, ICE, average CE and capacity retention of S-HC and T-HC electrodes in half-cell configuration.

HC sample	1st sod. (mAh g^{-1})	1st desod. (mAh g^{-1})	ICE (%)	2nd desod. (mAh g^{-1})	η_{CE} (%)	100th desod. (mAh g^{-1})	Capacity retention (%) (100th vs. 1st cycle)
1100–100	346	155	45.0	130	99.8	-	-
1100–32	340	235	69.1	173	99.5	-	-
1100–25	332	259	78.1	248	99.7	217	85
1000–25	336	277	82.0	272	99.9	256	93
900–25	341	265	77.9	257	99.7	244	93

properties, 1100–25 HC electrodes with mass loading of 5 mg cm^{-2} were tested in full cells (Fig. S5) using NVPF as cathode. The full cell delivers discharge capacities of 75 mAh g_{NVPF}^{-1} at 0.1C and 63 mAh g_{NVPF}^{-1} at 1C, maintaining stable operation for over 500 cycles.

The influence of pyrolysis temperature on the electrochemical performance of T-HCs is shown in Figs. 3a-c and 3g As evidenced earlier, 1000–25 HC exhibits the best electrochemical performance, both in the first cycle (Fig. 3a), where it delivers the highest ICE and largest capacity, and in the low-voltage plateau region (Fig. 3b) and upon long-term cycling (Fig. 3c). In particular, 1000–25 HC exhibits an ICE exceeding 82% and demonstrates excellent long-term performance at 0.1C, with a capacity of approximately 270 mAh g^{-1} over 200 cycles. In terms of rate capability, the 1000–25 material is also superior, showing 157 and 67 mAh g^{-1} at 1C and 5C, respectively (Fig. 3*g*). Surprisingly, 1100–25 HC outperforms 900–25 T-HC at high rates (from 1C and higher), but delivers lower capacity at lower rates. These results are in line with the CV results of T-HCs (Fig. S6), where 1100–25 delivers higher current density than 900–25 T-HC, and 1200–25 T-HC, indicating faster kinetics. In fact, 1200–25 T-HC exhibits a lower ICE compared with the other T-HCs, confirming that higher pyrolysis temperatures increase open porosity and deteriorate electrochemical performance. Therefore, as suggested in Fig. 3b, the high proportion of LVC contributes to improved electrochemical performance at high rates, contrary to the typical understanding that HVC offers better kinetics. The contributing factors to such a performance are explored later in this work.

The relationship between ICE and surface impurities was examined using XPS. Increasing temperatures reduce surface impurities (Fig. S2 and Table S1) but do not necessarily increase ICE, suggesting that ICE is not strictly related to surface impurity content. Figs. 3h–i show the BET SSA and pore size distribution of T-HCs, measured using Ar adsorption, which is suitable for detecting micropores within the carbon structure. The adsorption isotherms reveal that 1100–25 HC exhibits the highest adsorption volume at relatively low pressure, indicating the largest SSA and a greater presence of open micropores compared to other T-HC samples. In contrast, 1000–25 HC shows the lowest SSA and limited micro-/mesoporosity (Table 1), yet it achieves the highest ICE. This inverse relationship confirms that a lower SSA, particularly with fewer exposed micropores, helps reduce irreversible capacity loss caused by extensive SEI formation, thereby enhancing ICE. In conventional HCs, higher pyrolysis temperatures generally promote the closure of surface pores. However, in biomass-derived HCs, impurities play an additional role in regulating pore evolution. At high pyrolysis temperatures, impurities undergo crystallization and decomposition, as supported by the TEM results (Fig. 2a), while the coTGA–MS results in Fig. S3b indicate the release of CO_2. This process activates the carbon surface and generates more open pores, significantly altering the structural properties of the HC material. To further investigate the materials' porosity, CO_2 adsorption was used to complement Ar BET in probing ultramicropores (< 0.7 nm), which may not be fully accessible to Ar due to its larger kinetic diameter [63]. The CO_2 adsorption isotherms (Fig. S7) reveal that the 1000–25 HC exhibits the highest SSA among all samples (Table 1), indicating a pore structure containing a larger fraction of ultramicropores. These ultramicropores are largely inaccessible to the electrolyte but can provide favorable confined environments for Na^+ storage [28]. At lower temperatures, the impurities are more uniformly distributed (Fig. 2) and are associated with the formation of nanoscale pores and channels for Na^+ transport [64]. Such a pore architecture effectively enhances Na^+ diffusion within the carbon framework while limiting excessive electrolyte decomposition on the surface. Consequently, this combination of structural and morphological features not only yields high reversible capacity and improved reaction kinetics but also enhances the contribution from pore-filling capacity, as further elucidated by the theoretical investigation. Indeed, these evidences are supported by the CV results shown in Fig. S6, where 1000–25 HC delivers the highest current density. Additionally, the reduced micro-/mesoporosity and uniformly distribute impurities in 1000–25 HC contribute to the formation of a stable SEI, which significantly benefits the material's ICE and long-term electrochemical performance [65,66].

The (de)sodiation kinetics of T-HCs were first investigated using EIS combined with distribution of relaxation times (DRT) analysis during CV at selected states of charge, (Fig. S8). The DRT evolution of 1100–25 T-HC (Fig. S8a–c) shows that the dominant relaxation process shifts from a high time constant peak (I, ~10^2 s at 2 V) to a lower time constant peak (IV, ~10^{-2} s below 0.1 V) during sodiation (discharge), indicating a transition from slower surface-controlled processes to faster diffusion-related processes within the porous structure. This behavior also suggests that potential-driven charge storage processes play an important role during sodiation, consistently with previous reports [67]. The EIS spectra collected during the first four cycles (Fig. S8d) exhibit nearly identical impedance at 0.5 V and 0.1 V, suggesting stable interfacial behavior after the initial activation. Furthermore, comparison among different T-HCs (Fig. S8e) shows that 1000–25 exhibits the lowest impedance during both sodiation and desodiation, consistent with its superior electrochemical performance.

The (de)sodiation kinetics of the 1000–25 T-HC were further investigated to discern diffusion-controlled from surface-controlled charge in the probed range of scan rates [68–70]. Therefore, CV tests were conducted at scan rates (ν) of 0.05, 0.1, 0.2, 0.5, and 1 mV s^{-1}, as shown in Fig. 4a. The CV response at a scan rate of 0.5 mV s^{-1} is fitted as an example (Fig. 4b) to distinguish between the processes occurring in the HVC and the LVC regions. The relationship between log (I) and log (ν) for these processes is presented in Fig. 4c, based on (Eq. (1)) proposed by Lindström *et al.*, which is used to differentiate surface-controlled from diffusion-controlled kinetics:

$$I(\nu) = a\nu^b \quad \text{(Eq. 1)}$$

where I is the peak current, ν is the scan rate, b is the slope of the log (I) vs. log (ν) plot, and a is the intercept. Therefore, the b value is used to determine the kinetics of the charge storage process in 1000–25 HC. The b value serves as an indicator of the rate-limiting process: for a reversible, semi-infinite diffusion-controlled process, $b \approx 0.5$ [71]. In the case of 1000–25 HC, the region I, related to the LVC process, has a slope (b_1) of 0.4, consistent with diffusion-controlled behavior for reversible systems (typically around 0.5). The slightly lower b value is due to increased polarization at higher scan rates, which also reduces the peak current near the vertex potential. In contrast, a b value close to 1 indicates that region II, related to the HVC process, is not limited by semi-infinite diffusion, but rather exhibits surface-controlled kinetics.

Fig. 4d presents the 10th sodiation (discharge)/desodiation (charge) voltage profiles for all studied HCs, providing insight into the sodiation mechanism from a thermodynamic perspective. An enlarged view of the low-voltage region shows that the S-HC with the smallest particle size (i.

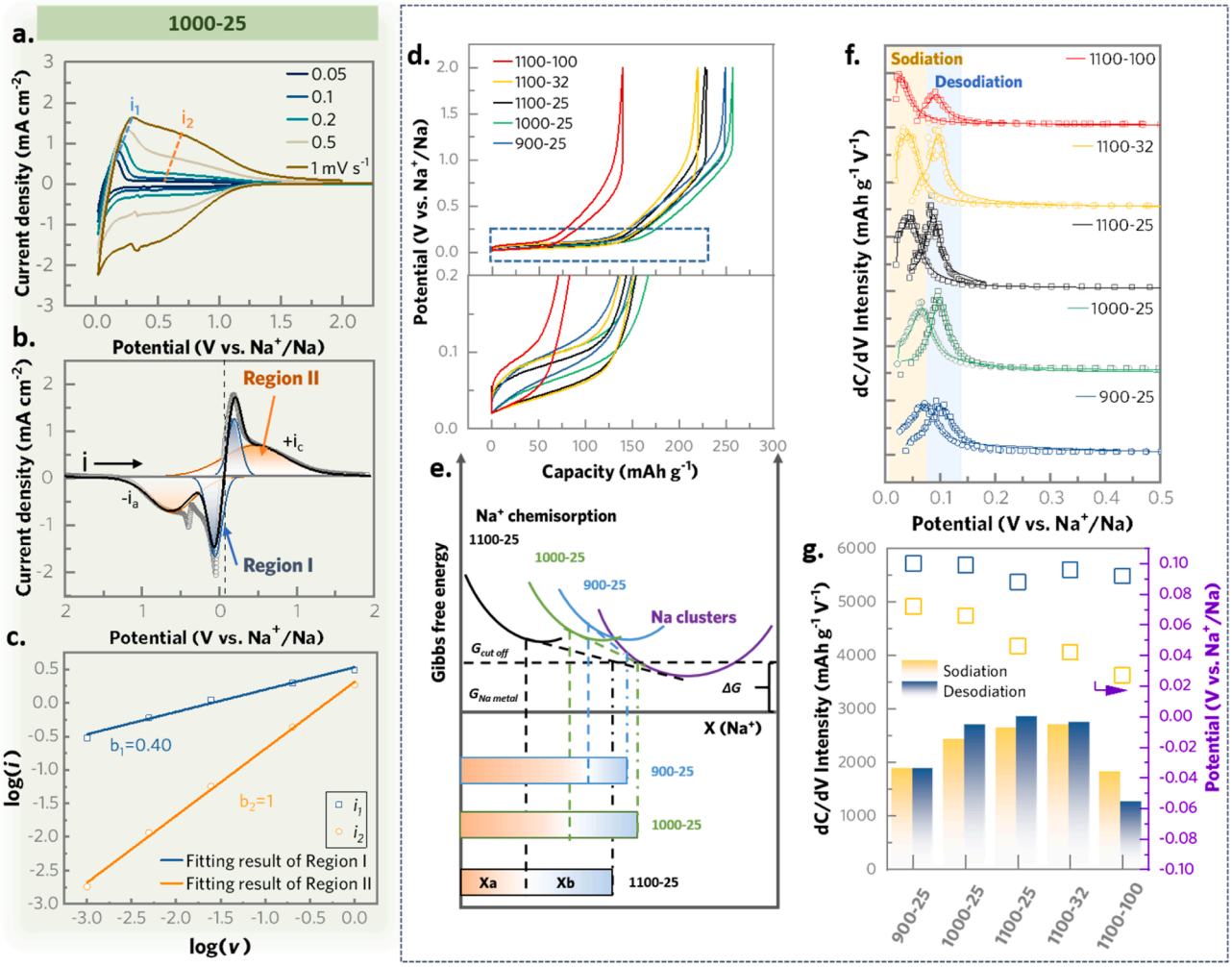

Fig. 4. Kinetic and thermodynamic analysis of (de)sodiation processes. a. CV curves for 1000–25 HC at different scan rates (0.05, 0.1, 0.2, 0.5, and 1 mV s^{-1}). **b.** Fitting results of the charge storage processes and **c.** calculated *b* value at the peak position by the relationship between log (*I*) vs. log (*v*). **d.** 10th galvanostatic sodiation (discharge) and desodiation (charge) curves. **e.** Schematic illustration of the thermodynamic analysis for Na^+ storage in T-HCs. **f.** First derivative results (dC/dV) from the galvanostatic cycling curve results of part d. **g.** Summary of dC/dV peak position and intensity corresponding to the results presented in panel f.

e., 1100–25) exhibits reduced overpotentials, which can be attributed to improved kinetics, as demonstrated in the CV (see Fig. 3f). Additionally, the data reveal that pyrolysis temperature significantly influences the plateau potential: lower pyrolysis temperatures yield higher plateau voltages. The reaction process firstly proposed as A↔B↔C, where A↔B represents the sloping voltage surface-controlled process, in which Na^+ is stored by chemisorption on HC, while B↔C corresponds to the diffusion-controlled process, occurring during the low voltage plateau, in which Na^+ is first inserted in the graphitic domains and, later, contributing to the generation of Na clusters. This relationship shows that these processes are not independent reactions but transform into one another during sodiation and desodiation. This interpretation aligns with previous *operando* ss ^{23}Na NMR studies, which showed that Na^+ in the sloping region gradually transitions into a metallic state as the plateau progresses. The signal corresponding to Na^+ decreases, while the Na^0 (metallic) signal increases and remains stable throughout the plateau region [39], supporting the mechanism of Na^+ chemisorption followed by metallic Na cluster formation.

The Na^+ storage mechanism in hazelnut shell-derived HC can be interpreted using thermodynamics, as schematically illustrated in Fig. 4e. This diagram illustrates the relationship between the Gibbs free energy and the Na^+ concentration (X(Na^+)) in HC, representing the evolution of Na's chemical potential during sodiation. At low Na^+ concentrations, Na^+ are chemisorbed onto defects, corresponding to the sloping voltage region of the voltage profile. This corresponds to the curves on the left side of the Gibbs free energy profile, where Na^+ is stabilized in specifically adsorbed states (Na^+ chemisorption). Each colored curve in Fig. 4e represents a different HC material synthesized at a specific pyrolysis temperature (900–25 (light blue), 1000–25 (green), and 1100–25 (black)). The Na^+ chemisorption curves differ based on structural disorder and defect density induced by pyrolysis. Higher pyrolysis temperatures (e.g., 1100 °C – black line) lead to more graphitized domains and fewer defect sites, thereby shifting the chemisorption curve downward to a lower Gibbs free energy state. As the Na^+ concentration increases, the system undergoes a phase transformation in which Na^+ begins to form quasi-metallic Na clusters associated with the low voltage plateau. The tangent dots lines between the Na^+ chemisorbed curves and the Na clusters curve (solid purple curve) mark the phase equilibrium between chemisorbed Na^+ and Na clusters. The intersection points (tangency points on the Na^+ chemisorption curves) indicate the Na concentration at which the system transitions from defect chemisorption to Na cluster formation. Below the plot, the bar graphs illustrate the capacity contributions from X_a (HVC), i.e., Na^+ chemisorption at defects in HC and X_b (LVC), i.e., Na cluster formation. The 900–25 HC, with higher defect concentration, has a broader HVC (X_a) and a smaller LVC region (X_b). The 1000–25 HC shows a better balance, with a higher LVC (X_b) due to the greater presence of pseudographitic domains. The 1100–25 HC shows a larger potential drop below the cut-off voltage,

reducing the effective LVC observed during cycling. This thermodynamic model aligns well with the galvanostatic profiles (Fig. 4d) and explains that increased graphitization promotes Na cluster formation at lower voltages, thereby extending the LVC. In contrast, lower temperatures favor Na^+ chemisorption at defects, thereby improving the sloping region but limiting overall capacity.

Fig. 4f presents the differential capacity curves (dC/dV) corresponding to the voltage profiles in Fig. 4d, offering new insights into the Na^+ storage mechanism. The potential peak could be taken as the reaction's potential in the plateau region. The difference in peak potential between sodiation and desodiation processes indicates the overpotential needed for the reactions, with a smaller difference signifying better kinetics. The HC with smaller particle sizes (1100–25 HC) exhibits increased peak intensity and reduced peak potential difference between sodiation and desodiation (see Fig. 4g), suggesting enhanced kinetics, as also observed with the CV experiments (see Fig. 3). The peak intensity is inversely related to the rate of potential change in the plateau region, while the area under the peak reflects the charge contribution of that region. Therefore, a higher intensity and larger area under galvanostatic conditions suggest slower potential variation, improved reaction efficiency, and increased LVC.

Regarding the effect of pyrolysis temperature, both the peak

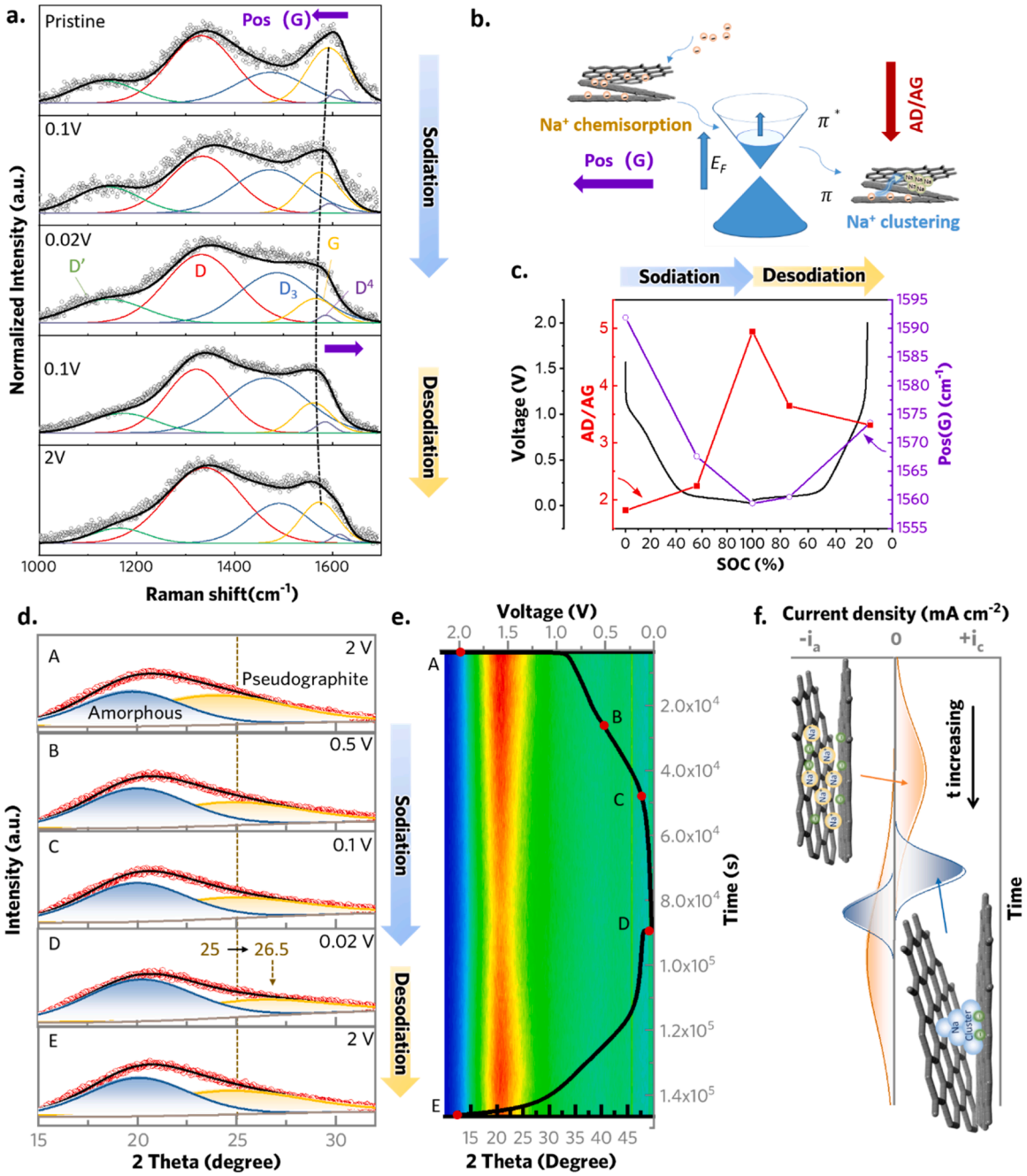

Fig. 5. ***Ex-situ*** **Raman and** ***Operando*** **XRD of 1000–25 T-HC, illustrating the structural evolution and Na-storage mechanism during (de)sodiation. a.** Ex-situ Raman spectra collected at different voltages. **b.** Schematic illustration of the electron-transfer process during sodiation. **c.** Raman analysis showing the structural evolution of HC, where the solid red squares represent the intensity ratio (A_D/A_G) and the open circles denote the position of the G-band shift at corresponding states of charge (SOC). **d.** Selected XRD patterns focusing on the (002) reflection and the corresponding deconvolution at different states of charge. **e.** Intensity of the (002) peak during the first sodiation (discharge) and desodiation (charge) cycle. **f.** Schematic of the sodiation mechanism.

intensity and area increase with temperature, indicating a greater capacity contribution from the plateau region. However, for T-HCs, increasing temperature also decreases peak potential, while the difference in peak potential between sodiation and desodiation increases with temperature, indicating a larger overpotential induced by higher pyrolysis temperature. Indeed, 900–25 HC and 1000–25 HC are the only two materials that exhibit a complete peak upon sodiation, suggesting that sodiation is not fully completed in the other HCs, consistent with the analysis in Fig. 4e. This incomplete sodiation process limits capacity, explaining why higher temperatures fail to improve specific capacity in 1100–25 HC despite increasing the LVC proportion.

3.3. Evolution of pseudographitic domains during electrochemical cycling

Ex-situ Raman spectroscopy was performed to investigate the structural evolution of 1000–25 HC during sodiation and desodiation (Fig. 5a-c). The Raman spectrum of 1000–25 T-HC can be deconvoluted into five components (Fig. 5a). The G-band (1560–1580 cm^{-1}) originates from the in-plane vibration of sp^2 C–C bonds, whereas the D-band (1320–1340 cm^{-1}) corresponds to defects or edge sites of graphitic domains [72,73]. During sodiation, the G-band gradually red-shifts and decreases in intensity. As schematically illustrated in Fig. 5b, this red-shift is associated with electron transfer from Na to the π antibonding orbitals of carbon, which weakens the C–C bonds and consequently increases the Fermi energy (E_F) of HC [74,75]. The intensity decreases of the G-band and concurrent increase of the D_3-band component indicate for an increasing structural disorder, consistent with Na insertion and the partial disruption of pseudographitic domains. Interestingly, as shown in Fig. 5c, the G-band evolution differs between the two voltage regions. In HVC, the G-band exhibits a pronounced red-shift, implying that electrons fill the π* orbitals and raise the Fermi level. In contrast, the G-band position in LVC does not show such a significant shift, while its intensity changed markedly. This behavior suggests that HVC correlates with electron transfer from Na to HC π* orbitals; however, in LVC, the electron transfer from HC to the Na clusters formed in HC with increased structural disorder.

In addition, *operando* X-ray diffraction (XRD) was performed to corroborate the structural changes observed in 1000–25 HC by Raman spectroscopy during the first (de)sodiation cycle. Previous *operando* XRD studies on HC anodes in SIBs have reported conflicting interpretations of the structure-performance relationship, which can largely be attributed to differences in HC microstructure among studies and to the intrinsically amorphous nature of HC that complicates signal identification and analysis [76]. Figs. 5d and 5e present the evolution of the (002) reflection at different states of charge. The deconvoluted reflection at around 20° 2θ-degrees corresponds to the amorphous HC, while the one at around 25°−26° 2θ-degrees corresponds to the ordered pseudographitic domains [77–80]. During the first sodiation process, the overall intensity of the (002) reflection decreases continuously (Fig. 5e), which is attributed to increasing Na^+ concentration within the carbon matrix. Simultaneously, the relative contribution of the ordered pseudographitic component decreases (Table S2), while the amorphous contribution increases. Notably, the amorphous fraction rises from ~45% to ~66% in the low-voltage plateau region (0.1–0.02 V; Fig. 5e, regions C and D), indicating progressive disordering of pseudographitic domains. This transformation is attributed to the formation of Na clusters within pores adjacent to pseudographitic layers, which disrupts local structural ordering.

The schematic in Fig. 5f summarizes this mechanism. In the high-voltage sloping region, Na^+ storage is dominated by chemisorption at defect sites. At lower voltages, diffusion-controlled Na clustering occurs within pores associated with pseudographitic domains, leading to reversible structural disordering. While pseudographitic domains are essential for accommodating Na clusters and improving low-voltage plateau capacity, excessive graphitization at higher temperatures reduces defect density and adsorption capacity. These results highlight that the balance between pseudographitic ordering and defects is critical for designing high-performance HC anodes for SIBs.

3.4. Theoretical investigation of porous regions in hard carbon

To shed light on Na storage in porous HC, we employed first-principles simulations based on DFT, including AIMD and analyses of charge density and electronic structure. This framework enables direct examination of Na-carbon interactions across curved graphene fragments and nanoporous domains.

Amorphous carbon frameworks have been generated using a molecular dynamics simulation implemented in LAMMPS. An initially random carbon arrangement was constructed with Packmol, melted at 3000 K, annealed, and then quenched to 300 K to form a densified sp^2/sp^3 network resembling experimentally observed HC microstructures. By adjusting the simulation cell volume, two carbons with distinct and experimentally relevant bulk densities were obtained. These structural models were subsequently relaxed with DFT and evolved through AIMD at 300 K for 15 ps, ensuring that the local bonding environments and pore geometries reached thermodynamically representative configurations.

The local coordination environment of Na within HC was resolved by evaluating the C–Na and Na–Na radial distribution functions for amorphous HC with bulk densities of 1.69 g cm^{-3} (low-porosity, high-density) and 1.32 g cm^{-3} (high-porosity, low-density), as shown in Fig. 6a–b. The porosity defined in these models reflects Na-accessible pores, beyond the open microporosity probed by Ar-SSA, consistent with CO_2-SSA measurements that capture ultramicroporous domains relevant to Na^+ storage. The C–Na RDFs show a pronounced first-shell peak at ~2.8–3.0 Å for both HCs, consistent with Na residing in proximity to disordered carbon motifs. Notably, the peak is sharper and more intense in the low-porosity HC, reflecting a tighter, more uniform local coordination environment imposed by the compact matrix. In contrast, the broader and attenuated peak in the high-porosity HC indicates greater structural heterogeneity and a wider distribution of Na–C distances, consistent with the presence of larger voids and more open pore channels. The Na–Na RDFs further distinguish how host density governs the spatial arrangement of Na. The high-porosity HC exhibits a more prominent first Na–Na correlation at ~3.5 Å, signifying enhanced ion–ion association and the onset of small Na-rich domains within the enlarged pore network. By comparison, the low-porosity HC largely suppresses Na–Na correlations, indicating that Na remains more isolated and preferentially stabilized by the carbon framework rather than by neighboring Na atoms.

The low-porosity (high-density) HC exhibits stronger and more localized charge redistribution around Na, indicative of enhanced Na–C electronic coupling under spatial confinement. In contrast, the high-porosity (low-density) HC shows more diffuse and weaker charge rearrangement, reflecting reduced confinement and weaker host–guest interactions in larger pore environments. These electronic trends correlate with the density-dependent Na coordination and clustering behavior observed in the RDF and diffusivity analyses.

Beyond structural analysis, AIMD simulations enable direct quantification of Na mobility within HCs of different densities. We extracted self-diffusion coefficients of 5.17×10^{-7} m^2 s^{-1} for the denser carbon and 5.05×10^{-6} m^2 s^{-1} for the lower-density carbon from the mean squared displacement of Na atoms. The nearly order-of-magnitude increase in diffusivity in the less-dense structure underscores the pivotal roles of free volume and pore connectivity in regulating Na transport. In low-porosity HC, Na diffusion is strongly constrained by the compact carbon framework and the prevalence of smaller, isolated micropores. Na atoms preferentially occupy energetically favorable sites near curved graphene fragments and defects, where strong Na–C interactions stabilize isolated ions and suppress long-range motion. Consequently, Na insertion occurs through the sequential filling of small pores with limited Na–Na interactions and minimal clustering. In contrast, the

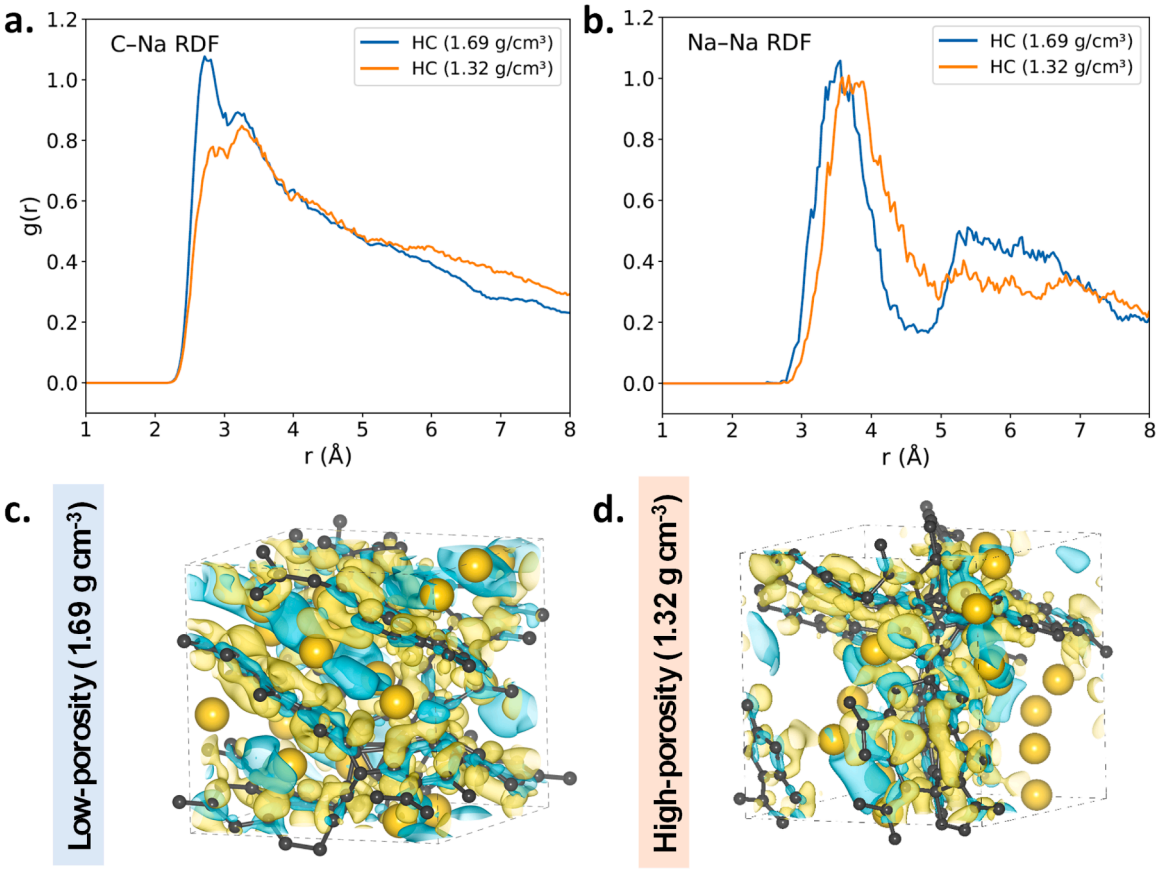

Fig. 6. Radial distribution functions and charge density differences induced by sodium insertion in HC with different bulk densities. a. C–Na and **b.** Na–Na RDFs extracted from AIMD trajectories for HC structures with bulk densities of 1.69 g cm^{-3} (**Fig. S9a**, lower porosity) and 1.32 g cm^{-3} (**Fig. S9b**, higher porosity). Charge density difference maps induced by Na insertion in HC with bulk densities of **c.** 1.32 g cm^{-3} (high-porosity) and **d.** 1.69 g cm^{-3} (low-porosity). Charge accumulation and depletion regions are shown in yellow and blue, respectively.

significantly higher diffusivity observed in high-porosity HC reflects the presence of larger, more interconnected nanoporous domains. These expanded pores provide sufficient space for Na atoms to migrate more freely and explore a broader configurational landscape. Once the primary adsorption sites are occupied, additional Na can enter these larger voids, where Na–Na interactions become increasingly favorable. This transition facilitates the formation of Na-rich regions and local clustering, which is consistent with the enhanced Na–Na correlations observed in the RDF analysis.

Together, diffusivity trends and structural correlations reveal a clear porosity-dependent Na-storage mechanism. Low-porosity HC favors localized, defect- and surface-dominated Na storage with limited mobility, corresponding to enhanced HVC. By contrast, high-porosity HC promotes pore filling, followed by Na clustering in larger cavities, thereby increasing LVC. The ex-situ SAXS results (Fig. S10) provide direct evidence for this pore-filling process. During sodiation, the scattering intensity in the microporous region decreases due to the reduced electron-density contrast between the carbon matrix and the nanopores. Upon desodiation, the scattering intensity partially recovers, indicating reversible nanopore occupation. Combined with the SAXS results, this atomistic picture explains the electrochemical behavior shown in Fig. 3 and the structural observations in Fig. S9. Specifically, the 900–25 HC sample exhibits a higher bulk density and lower nanoscale porosity, as indicated by CO_2-BET measurements probing micropores. As a result, 900–25 HC delivers a higher HVC dominated by surface/defect-related Na^+ adsorption, but a suppressed LVC due to incomplete Na-cluster formation within the limited pore volume. In contrast, 1000–25 HC shows a higher micropore volume and overall porosity, as determined by CO_2-BET analysis, corresponding to a lower bulk density. This more open pore structure reduces the contribution from HVC but strongly facilitates Na filling and clustering, resulting in a significantly enhanced LVC.

To gain insight into the electronic response of the HC host upon Na insertion, the charge-density difference for both HC densities has been analyzed, as shown in Fig. 6c-d. The charge-density difference highlights regions of charge accumulation and depletion induced by Na incorporation. This analysis provides a complementary electronic perspective on the structural information obtained from the RDFs, allowing direct assessment of how confinement and pore topology influence Na–carbon interactions.

In low-porosity HC (1.69 g cm^{-3}; Fig. 6c), the charge-density difference maps reveal stronger and more localized charge rearrangements around Na atoms. The compact carbon framework forces Na into close proximity to surrounding carbon sites, thereby enhancing Na–C electronic coupling. Pronounced charge accumulation adjacent to Na atoms, accompanied by clear charge depletion at the Na centers, indicates significant electron transfer from Na to nearby carbon π-like states or defect-associated orbitals. This behavior reflects a higher degree of Na ionization under spatial confinement. In addition, the surrounding carbon network exhibits stronger polarization, consistent with intensified electrostatic interactions and local hybridization in tightly confined environments. This electronic response is fully consistent with the ex-situ Raman results in Fig. 5a, where the G-band redshifts in the LVC region indicate filling of the carbon π* orbitals. These electronic features align with the RDF analysis, which shows a sharper, more intense first-shell Na–C coordination peak in the dense carbon, confirming stronger, more localized Na–C interactions. Together, these observations indicate that Na is more strongly bound and electronically coupled to the host

framework in compact pore structures. These electronic features are consistent with the RDF results, which show a stronger and more well-defined first-shell Na–C coordination peak in the dense carbon. Together, they indicate that Na is more strongly bound and electronically coupled to the host when confined within compact pore structures.

In contrast, high-porosity HC (1.32 g cm^{-3}; Fig. 6d) exhibits more diffuse and weaker charge redistribution upon Na insertion. The larger free volume and more open pore network allow Na atoms to reside farther from the carbon walls, reducing direct Na–C overlap. As a result, the charge-density difference maps show reduced charge transfer, broader and less localized accumulation regions, and a weaker overall polarization of the carbon framework. These features indicate a weaker bound Na environment with diminished electronic confinement. This behavior aligns with the broader and lower-intensity Na–C coordination peaks observed in the RDFs, as well as the enhanced Na–Na correlations in the high-porosity structure. Once the primary adsorption sites are occupied, the larger pores can accommodate multiple Na atoms with relatively weak host interactions, facilitating Na–Na association and clustering rather than strong Na–C bonding.

Taken together with the RDF and diffusivity analyses, the charge-density difference results demonstrate that Na storage in HC is governed by a strong coupling between geometric confinement and the strength of electronic interactions. Low-porosity HC promotes localized Na storage characterized by strong Na–C binding, enhanced charge transfer, and limited Na mobility. In contrast, high-porosity HC supports weaklier bound and mobile Na, enabling pore filling and the emergence of Na-rich clusters within larger cavities. These porosity-dependent electronic responses have direct implications for the Na storage mechanism and voltage behavior. Stronger polarization and charge transfer in low-porosity HCs favor higher-potential, adsorption-dominated storage, whereas weaker host–guest interactions in high-porosity HCs support clustering and metallic-like Na behavior at deeper sodiation levels, contributing to plateau formation.

3.5. Strategies for maintaining high-rate capacity

To understand the contributions of HVC and LVC at different current densities, additional rate capability tests and analyses were conducted (Fig. S11a). The proportions of HVC and LVC under different current densities are also illustrated (Fig. 7a-c).

First, focusing on the HVC region (orange bars), it is observed that its contribution remains relatively stable across different current densities. In contrast, the LVC region (blue bars) is almost completely depleted at high current densities, leading to a rapid decline in capacity, as observed in Fig. 3e, and indicating that the LVC's contribution limits rate performance. When comparing 900–25, 1000–25, and 1100–25 HCs, the material carbonized at 1000 °C provides the highest LVC contribution at all current densities. This observation is consistent with the improved rate performance and lower impedance of 1000–25 HC and suggests that maintaining LVC capacity is crucial for delivering high-rate performance.

Fig. 7d illustrates the thermodynamic model based on Gibbs free energy theory. When examining rate performance, the process deviates from thermodynamic stability due to kinetic factors during sodiation and desodiation. At higher current densities, the reactions proceed more rapidly, accompanied by increased polarization. These result in a

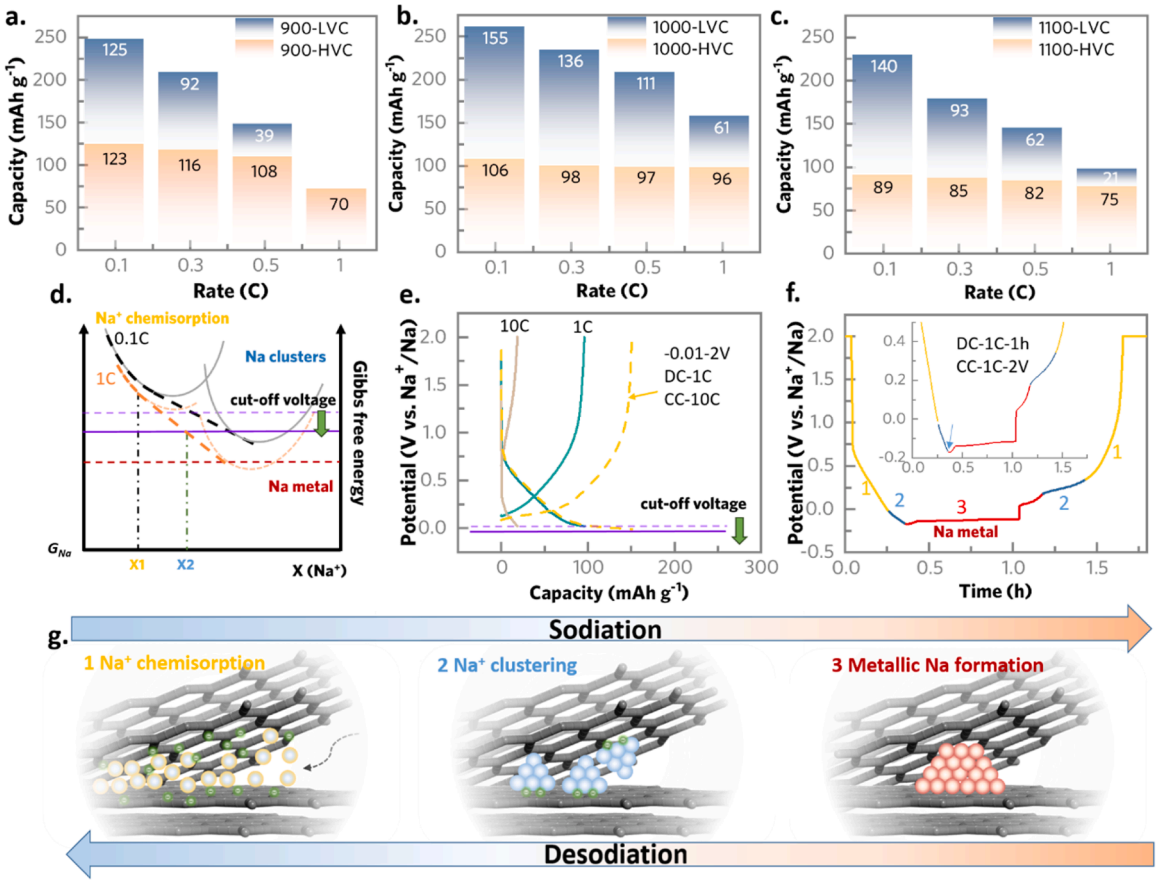

Fig. 7. Rate-capacity analysis and mechanism of (de)sodiation processes at high rates. a-c. Calculated capacity of the sloping (HVC) and low voltage plateau (LVC) regions at different C-rates of T-HCs. **d.** Analysis of the influence of (de)sodiation rates based on the Gibbs free energy of HC. **e.** Voltage profiles of 1100–25 T-HC at different current densities and influence of lower cut-off voltages, corresponding to the analysis in part d. **f.** Applying a current density at 1C (DC) and 1C (CC) below 0 V vs. Na^+/Na. **g.** Schematic representation of the Na state during the processes shown in part f, with a particular focus on the Na stable state.

sodiation/desodiation curve (high-current-density light-orange-dot curves) that significantly deviates from the thermodynamic curve (low-current-density gray-dot curve). The diverging curve (orange-dot lines) at high current densities (such as 1C) exhibits a larger overpotential than at lower current densities (0.1C, see black-dot line), resulting in lower capacity due to the lower voltage of LVC falling below the cut-off voltage (see the light purple-dot line with respect to the orange-dot line in Fig. 7d). To further investigate this behavior, following this protocol, 1100–25 HC, exhibiting a low capacity contribution in the low voltage plateau at 1C (green line); sodiated (discharged) to 0.02 V at 0.1C and then desodiated (charged) at 1C (green dotted line in Fig. S11b). 1100–25 HC delivers a desodiation capacity of around 240 mAh g^{-1}, which is slightly lower than that observed at 0.1C (253 mAh g^{-1}, blue line), indicating that high current densities do not inhibit desodiation.

The same protocol was applied for desodiation (charging) at different current densities, but with the cut-off voltage lowered to −0.01 V vs. Na^+/Na (Fig. 7e). The results show a similar trend to that above, with the delivered capacity under 1C sodiation (discharge) and 10C desodiation (charge) conditions (yellow dot line) exceeding that obtained when cycling continuously at either 10C (brown line) or 1C (green line). Specifically, decreasing the cut-off voltage during sodiation at high current to −0.01 V vs. Na^+/Na led to a notable improvement: for example, 1100–25 HC, which originally delivered 21 mAh g^{-1} on the low voltage plateau at 10C, increased to 150 mAh g^{-1} when sodiated at 1C and desodiated at 10C. This indicates that higher rates require lower potentials for effective sodiation on the low-voltage plateau. The larger plateau region in 1100–25 HC reflects superior sodiation kinetics, as also supported by the CV results. Consequently, a lower overpotential is needed, enabling greater capacity retention at high current densities—explaining why a higher LVC proportion leads to improved rate performance.

The thermodynamic model depicted in Fig. 7d also suggests that at higher rates, the low voltage plateau occurs at a potential below that of metallic Na (red dot line), as observed in Fig. 7f. To investigate the formation of Na species at this low potential of −0.01 V vs. Na^+/Na, the 1100–25 HC was sodiated at 0.1C for 15 h, as shown in Fig. S11c. During sodiation, the plateau process (stage 2) occurs, followed by the formation of metallic Na (stage 3), as outlined in the scheme of Fig. 7d Fig. 7f shows similar results when discharged and charged at 1C. In this case, the contribution of the short, low-voltage plateau (stage 2) increases during the charging process. This suggests that metallic Na (stage 3) formed within the HC structure may transform from Na clusters back to Na^+ upon desodiation, showing a reversible process. This is consistent with the thermodynamic model (Fig. 7d), where at fast sodiation rates (e.g., 1C), Na clustering occurs at a lower potential, leading to a decreased specific capacity of HC. This behavior highlights the kinetic and thermodynamic dynamics of Na storage in HC, where faster sodiation rates favor the formation of metallic Na over Na clusters, decreasing the overall capacity and efficiency of the storage process.

4. Conclusion

This work systematically investigated the sodiation and desodiation behavior of hazelnut shell–derived HC synthesized via a sustainable route, with the aim of elucidating its Na storage mechanism and structure–performance relationships for SIBs. Comprehensive analyses of structure, morphology, composition, impurity distribution, electrochemical performance, structural evolution, and theoretical simulations lead to the following conclusions:

i. Smaller HC particles exhibit enhanced Na^+ transport kinetics, resulting in higher specific capacity and improved long-term cycling stability. The shortened diffusion pathways and increased electrochemically active interfaces also promote a higher contribution from the low-voltage plateau capacity during sodiation (discharge).
ii. Higher pyrolysis temperatures induce crystallization and aggregation of inorganic impurities, which increase the SSA and promote thicker SEI formation, thereby hindering the sodiation process. In contrast, uniformly distributed impurities achieved by lower pyrolysis temperature regulate pore formation within the carbon framework and contribute to improved reversible Na storage.
iii. Among the studied HC samples, 1000–25 HC exhibits the best overall electrochemical performance, delivering a capacity of 270 mAh g^{-1} at 0.1C and maintaining stable cycling for over 200 cycles. This superior behavior originates from its optimized pore structure, which provides higher internal porosity to support Na clustering while limiting excessive surface-accessible porosity, thereby maximizing the low-voltage plateau contribution.
iv. The Na^+ storage mechanism proceeds via two distinct regimes. The sloping region is governed by chemisorption-controlled kinetics, associated with Na^+ chemisorption at defect sites. In contrast, the low-voltage plateau is dominated by diffusion-controlled Na clustering within pores adjacent to pseudographitic layers, accompanied by reversible structural disordering of the pseudographitic framework. Metallic-like Na clusters form reversibly during deep sodiation and transform back upon desodiation.

Overall, this work provides design guidelines for biomass-derived HC anodes, demonstrating that impurity distribution controls the pore structure of HCs and offers a simple, sustainable strategy for HC synthesis. The combined kinetic and thermodynamic analyses provide mechanistic insight into Na^+ storage in biomass-derived HCs and establish a practical framework for designing high-performance hard carbon anodes for next-generation sodium-ion batteries.

CRediT authorship contribution statement

Shuting Zhang: Writing – review & editing, Writing – original draft, Visualization, Methodology, Investigation, Data curation. **Mohsen Sotoudeh:** Writing – review & editing, Investigation, Data curation. **Robert Leiter:** Writing – review & editing, Investigation, Data curation. **Wenbo Wang:** Writing – original draft, Formal analysis. **Lukas Pfeiffer:** Writing – review & editing, Investigation. **Simon Fleischmann:** Writing – review & editing, Supervision. **Peter Axmann:** Writing – review & editing, Supervision. **Dominic Bresser:** Writing – review & editing, Supervision. **Maider Zarrabeitia:** Writing – review & editing, Supervision, Project administration, Methodology, Investigation, Funding acquisition, Formal analysis, Conceptualization. **Stefano Passerini:** Writing – review & editing, Supervision, Methodology, Funding acquisition, Formal analysis, Conceptualization.

Declaration of competing interest

The authors declare that they have no known competing financial interests or personal relationships that could have appeared to influence the work reported in this paper. Given his role as Editorial Board Member of Energy Storage Materials, Simon Fleischmann had no involvement in the peer review of this article and had no access to information regarding its peer review. Full responsibility for the editorial process for this article was delegated to another journal editor.

Acknowledgements

The authors acknowledge support from the project Transition Transfer (03XP05338), funded by the Bundesministerium für Forschung, Technologie und Raumfahrt (BMFTR), and basic funding from the Helmholtz Gemeinschaft. Mr. Luciano Andrea Marchini and Mr.

Andrea Passerini are kindly acknowledged for providing the raw bio-waste material (hazelnut shells). S.Z. gratefully acknowledges the financial support from the Chinese Scholarship Council (CSC). R.L. and S.F. acknowledge funding from BMFTR in the NanoMatFutur program (03XP0423). DFT and AIMD simulations contributed to research at CELEST (Center for Electrochemical Energy Storage Ulm-Karlsruhe) and were funded by the German Research Foundation (DFG) under Project ID 390874152 (POLiS Cluster of Excellence). Computer time provided by the state of Baden-Württemberg through bwHPC and the German Research Foundation (DFG) through grant no INST 40/575–1 FUGG (JUSTUS 2 cluster) is gratefully acknowledged by M.S.

Supplementary materials

Supplementary material associated with this article can be found, in the online version, at doi:10.1016/j.ensm.2026.105091.

Data availability

Data will be made available on request.

References

[1] W. Lu, Z. Wang, S. Zhong, Sodium-ion battery technology: advanced anodes, cathodes and electrolytes, J. Phys. Conf. Ser. 2109 (2021) 012004, https://doi.org/10.1088/1742-6596/2109/1/012004.
[2] K. Chayambuka, G. Mulder, D. Danilov, P. Notten, From Li-ion batteries toward Na-ion chemistries: challenges and opportunities, Adv. Energy. Mater. 10 (2020) 2001310, https://doi.org/10.1002/aenm.202001310.
[3] Q. Wen, C. Li, Q. Chen, P. Zhao, C. Wu, X. Wu, S.-L. Chou, Carbon engineering for sodium batteries: multi-role architectures bridging material design and hybrid system innovation, Chem. Soc. Rev. 54 (2025) 9317–9369, https://doi.org/10.1039/D5CS00515A.
[4] Critical raw materials - European Commission (n.d.), https://single-market-economy.ec.europa.eu/sectors/raw-materials/areas-specific-interest/critical-raw-materials_en, July 7, 2024 (accessed.
[5] T. Vranken, Critical raw materials in Li-ion batteries, (n.d.). https://innoenergy.com/uploads/2023/01/critical-raw-materials-in-li-ion-batteries.pdf.
[6] CRMs_for_Strategic_Technologies_and_Sectors_in_the_EU_2020.pdf (n.d.), https://rmis.jrc.ec.europa.eu/uploads/CRMs_for_Strategic_Technologies_and_Sectors_in_the_EU_2020.pdf, July 7, 2024. accessed.
[7] C. Vaalma, D. Buchholz, M. Weil, S. Passerini, A cost and resource analysis of sodium-ion batteries, Nat. Rev. Mater. 3 (2018) 1–11, https://doi.org/10.1038/natrevmats.2018.13.
[8] P.K. Nayak, L. Yang, W. Brehm, P. Adelhelm, From lithium-ion to sodium-ion batteries: advantages, challenges, and surprises, Angew. Chem. Int. Ed 57 (2018) 102–120, https://doi.org/10.1002/anie.201703772.
[9] JMEV | about us (n.d.), https://en.jmev.com/about/(accessed, December 9, 2024.
[10] M.D. Slater, D. Kim, E. Lee, C.S. Johnson, Sodium-ion batteries, Adv. Funct. Mater. 23 (2013) 947–958, https://doi.org/10.1002/adfm.201200691.
[11] S. Ong, V.L. Chevrier, G. Hautier, A. Jain, C. Moore, S. Kim, X. Ma, G. Ceder, Voltage, stability and diffusion barrier differences between sodium-ion and lithium-ion intercalation materials, Energy. Env. Sci. 4 (2011) 3680–3688, https://doi.org/10.1039/C1EE01782A.
[12] C. Huang, J. Yin, W. Shi, Y. Cheng, X. Xu, Recent advances of tailoring defects and pores in hard carbon for sodium storage, Mater. Today Energy 40 (2024) 101501, https://doi.org/10.1016/j.mtener.2024.101501.
[13] J.M. Bray, C.L. Doswell, G.E. Pavlovskaya, L. Chen, B. Kishore, H. Au, H. Alptekin, E. Kendrick, M.-M. Titirici, T. Meersmann, M.M. Britton, Operando visualisation of battery chemistry in a sodium-ion battery by 23Na magnetic resonance imaging, Nat. Commun. 11 (2020) 2083, https://doi.org/10.1038/s41467-020-15938-x.
[14] L. Wu, D. Buchholz, C. Vaalma, G.A. Giffin, S. Passerini, Apple-biowaste-derived hard carbon as a powerful anode material for Na-ion batteries, ChemElectroChem 3 (2016) 292–298, https://doi.org/10.1002/celc.201500437.
[15] Z. Zeng, Y. Mao, Z. Hu, K. Chen, Q. Huang, Y. Song, Z. Wu, P. Zhang, T. Chen, X. Guo, Research progress and commercialization of biologically derived hard carbon anode materials for sodium-ion batteries, Ind. Eng. Chem. Res. 62 (2023) 15343–15359, https://doi.org/10.1021/acs.iecr.3c00818.
[16] M.A. Cusenza, S. Longo, F. Guarino, M. Cellura, Energy and environmental assessment of residual bio-wastes management strategies, J. Clean. Prod. 285 (2021) 124815, https://doi.org/10.1016/j.jclepro.2020.124815.
[17] V. Molahalli, A. Sharma, K. Bijapur, G. Soman, N. Chattham, G. Hegde, Low-cost bio-waste carbon nanocomposites for sustainable electrochemical devices: a systematic review, Mater. Today Commun. 38 (2024) 108034, https://doi.org/10.1016/j.mtcomm.2024.108034.
[18] A. Baldinelli, X. Dou, D. Buchholz, M. Marinaro, S. Passerini, L. Barelli, Addressing the energy sustainability of biowaste-derived hard carbon materials for battery electrodes, Green. Chem. 20 (2018) 1527–1537, https://doi.org/10.1039/C8GC00085A.
[19] J. Ou, Y. Zhang, L. Chen, Q. Zhao, Y. Meng, Y. Guo, D. Xiao, Nitrogen-rich porous carbon derived from biomass as a high performance anode material for lithium ion batteries, J. Mater. Chem. A 3 (2015) 6534–6541, https://doi.org/10.1039/C4TA06614F.
[20] W. Lv, F. Wen, J. Xiang, J. Zhao, L. Li, L. Wang, Z. Liu, Y. Tian, Peanut shell derived hard carbon as ultralong cycling anodes for lithium and sodium batteries, Electrochim. Acta 176 (2015) 533–541, https://doi.org/10.1016/j.electacta.2015.07.059.
[21] X. Dou, I. Hasa, M. Hekmatfar, T. Diemant, R.J. Behm, D. Buchholz, S. Passerini, H. Pectin, O. Lignin?, Impact of the biowaste source on the performance of hard carbons for sodium-ion batteries, ChemSusChem 10 (2017) 2668–2676, https://doi.org/10.1002/cssc.201700628.
[22] L. Bottoni, H. Darjazi, L. Sbrascini, A. Staffolani, S. Gabrielli, G. Pastore, A. Tombesi, F. Nobili, Electrochemical characterization of charge storage at anodes for sodium-ion batteries based on corncob waste-derived hard carbon and binder, ChemElectroChem 10 (2023) e202201117, https://doi.org/10.1002/celc.202201117.
[23] Y. Yan, G. Chen, W. Liu, M. Qu, Z. Xie, F. Wang, Pre-carbonization for regulating sucrose-based hard carbon pore structure as high plateau capacity sodium-ion battery anode, J. Energy Stor. 104 (2024) 114590, https://doi.org/10.1016/j.est.2024.114590.
[24] C. Wu, Y. Yang, Y. Zhang, H. Xu, X. He, X. Wu, S. Chou, Hard carbon for sodium-ion batteries: progress, strategies and future perspective, Chem. Sci. 15 (2024) 6244–6268, https://doi.org/10.1039/d4sc00734d.
[25] B. Lu, C. Lin, H. Xiong, C. Zhang, L. Fang, J. Sun, Z. Hu, Y. Wu, X. Fan, G. Li, J. Fu, D. Deng, Q. Wu, Hard-carbon negative electrodes from biomasses for sodium-ion batteries, Molecules 28 (2023) 4027, https://doi.org/10.3390/molecules28104027.
[26] Y. Wan, Y. Liu, D. Chao, W. Li, D. Zhao, Recent advances in hard carbon anodes with high initial coulombic efficiency for sodium-ion batteries, Nano Mater. Sci. 5 (2023) 189–201, https://doi.org/10.1016/j.nanoms.2022.02.001.
[27] T. Zhang, T. Zhang, F. Wang, F. Ran, Pretreatment process before heat pyrolysis of plant-based precursors paving way for fabricating high-performance hard carbon for sodium-ion batteries, ChemElectroChem 10 (2023), https://doi.org/10.1002/celc.202300442.
[28] H. Moon, A. Innocenti, H. Liu, H. Zhang, M. Weil, M. Zarrabeitia, S. Passerini, Bio-waste-derived hard carbon anodes through a sustainable and cost-effective synthesis process for sodium-ion batteries, ChemSusChem 16 (2023) e202201713, https://doi.org/10.1002/cssc.202201713.
[29] Effects of natural hard shell particles on physical, chemical, mechanical and thermal properties of composites. https://doi.org/10.1177/09673911211020717.
[30] Life-cycle cost analysis (LCCA) | WBDG - whole building design guide, (n.d.) (accessed, https://www.wbdg.org/resources/life-cycle-cost-analysis-lcca, June 2, 2025 (accessed.
[31] Y. Wen, K. He, Y. Zhu, F. Han, Y. Xu, I. Matsuda, Y. Ishii, J. Cumings, C. Wang, Expanded graphite as superior anode for sodium-ion batteries, Nat. Commun. 5 (2014) 4033, https://doi.org/10.1038/ncomms5033.
[32] D. Cheng, X. Zhou, H. Hu, Z. Li, J. Chen, L. Miao, X. Ye, H. Zhang, Electrochemical storage mechanism of sodium in carbon materials: a study from soft carbon to hard carbon, Carbon N Y 182 (2021) 758–769, https://doi.org/10.1016/j.carbon.2021.06.066.
[33] C. Bommier, T.W. Surta, M. Dolgos, X. Ji, New mechanistic insights on Na-ion storage in nongraphitizable carbon, Nano. Lett. 15 (2015) 5888–5892, https://doi.org/10.1021/acs.nanolett.5b01969.
[34] L. Sun, J. Li, L. Wang, E. Li, W. Huang, High temperature induced abundant closed nanopores for hard carbon as high-performance sodium-ion batteries anodes, J. Power Sources 624 (2024) 235474, https://doi.org/10.1016/j.jpowsour.2024.235474.
[35] Y. Zeng, J. Yang, H. Yang, Y. Yang, J. Zhao, Bridging microstructure and sodium-ion storage mechanism in hard carbon for sodium ion batteries, ACS Energy Lett. 9 (2024) 1184–1191, https://doi.org/10.1021/acsenergylett.3c02751.
[36] Z. Wang, X. Feng, Y. Bai, H. Yang, R. Dong, X. Wang, H. Xu, Q. Wang, H. Li, H. Gao, C. Wu, Probing the energy storage mechanism of quasi-metallic Na in hard carbon for sodium-ion batteries, Adv. Energy Mater. 11 (2021) 2003854, https://doi.org/10.1002/aenm.202003854.
[37] J.S. Weaving, A. Lim, J. Millichamp, T.P. Neville, D. Ledwoch, E. Kendrick, P. F. McMillan, P.R. Shearing, C.A. Howard, D.J.L. Brett, Elucidating the sodiation mechanism in hard carbon by Operando Raman spectroscopy, ACS Appl. Energy Mater. 3 (2020) 7474–7484, https://doi.org/10.1021/acsaem.0c00867.
[38] Y. Jin, S. Sun, M. Ou, Y. Liu, C. Fan, X. Sun, J. Peng, Y. Li, Y. Qiu, P. Wei, Z. Deng, Y. Xu, J. Han, Y. Huang, High-performance hard carbon anode: tunable local structures and sodium storage mechanism, ACS Appl. Energy Mater. 1 (2018) 2295–2305, https://doi.org/10.1021/acsaem.8b00354.
[39] J.M. Stratford, P.K. Allan, O. Pecher, P.A. Chater, C.P. Grey, Mechanistic insights into sodium storage in hard carbon anodes using local structure probes, Chem. Commun. 52 (2016) 12430–12433, https://doi.org/10.1039/C6CC06990H.
[40] A. Vasileiadis, Y. Li, Y. Lu, Y.-S. Hu, M. Wagemaker, Role of defects, pores, and interfaces in deciphering the Alkali metal storage mechanism in hard carbon, ACS Appl. Energy Mater. 6 (2023) 127–140, https://doi.org/10.1021/acsaem.2c02591.
[41] K.Z. Sasmoko, M. Malik, U. Awan, W. Handayani, M.K. Jabor, M. Asif, Environmental effects of bio-waste recycling on industrial circular economy and eco-sustainability, Recycling 7 (2022) 60, https://doi.org/10.3390/recycling7040060.
[42] G. Sonu, D. Pathania, A. R, S. Rustagi, Y.S. Huh, V.K. Gupta, A. Kaushik, V. Chaudhary, Agro-waste to sustainable energy: a green strategy of converting

agricultural waste to nano-enabled energy applications, Sci. Total Env. 875 (2023) 162667, https://doi.org/10.1016/j.scitotenv.2023.162667.
[43] M.C. Biesinger, Accessing the robustness of adventitious carbon for charge referencing (correction) purposes in XPS analysis: insights from a multi-user facility data review, Appl. Surf. Sci. 597 (2022) 153681, https://doi.org/10.1016/j.apsusc.2022.153681.
[44] Z. Wang, Y. Wang, B. Py, A. Maradesa, J. Liu, T.H. Wan, M. Saccoccio, F. Ciucci, DRTtools: freely accessible distribution of relaxation times analysis for electrochemical impedance spectroscopy, ACS Electrochem. 1 (2025) 2680–2689, https://doi.org/10.1021/acselectrochem.5c00334.
[45] P. Hohenberg, W. Kohn, Inhomogeneous electron gas, Phys. Rev. 136 (1964) B864–B871, https://doi.org/10.1103/PhysRev.136.B864.
[46] W. Kohn, L.J. Sham, Self-consistent equations including exchange and correlation effects, Phys. Rev. 140 (1965) A1133–A1138, https://doi.org/10.1103/PhysRev.140.A1133.
[47] D. Saurel, J. Segalini, M. Jauregui, A. Pendashteh, B. Daffos, P. Simon, M. Casas-Cabanas, A SAXS outlook on disordered carbonaceous materials for electrochemical energy storage, Energy Stor. Mater 21 (2019) 162–173, https://doi.org/10.1016/j.ensm.2019.05.007.
[48] P.E. Blöchl, Projector augmented-wave method, Phys. Rev. B 50 (1994) 17953–17979, https://doi.org/10.1103/PhysRevB.50.17953.
[49] J.P. Perdew, K. Burke, M. Ernzerhof, Generalized gradient approximation made simple, Phys. Rev. Lett. 77 (1996) 3865–3868, https://doi.org/10.1103/PhysRevLett.77.3865.
[50] Effect of the damping function in dispersion corrected density functional theory - Grimme - 2011, J. Comput. Chem. -. Wiley. Online. Libr (December 16, 2025) (n. d.), https://onlinelibrary.wiley.com/doi/10.1002/jcc.21759 (accessed.
[51] H.J. Monkhorst, J.D. Pack, Special points for Brillouin-zone integrations, Phys. Rev. B 13 (1976) 5188–5192, https://doi.org/10.1103/PhysRevB.13.5188.
[52] A.P. Thompson, H.M. Aktulga, R. Berger, D.S. Bolintineanu, W.M. Brown, P. S. Crozier, P.J. in 't Veld, A. Kohlmeyer, S.G. Moore, T.D. Nguyen, R. Shan, M. J. Stevens, J. Tranchida, C. Trott, S.J. Plimpton, LAMMPS - a flexible simulation tool for particle-based materials modeling at the atomic, meso, and continuum scales, Comput. Phys. Commun. 271 (2022) 108171, https://doi.org/10.1016/j.cpc.2021.108171.
[53] L. Martínez, R. Andrade, E.G. Birgin, J.M. Martínez, PACKMOL: a package for building initial configurations for molecular dynamics simulations, J. Comput. Chem. 30 (2009) 2157–2164, https://doi.org/10.1002/jcc.21224.
[54] N.A. Marks, Generalizing the environment-dependent interaction potential for carbon, Phys. Rev. B 63 (2000) 035401, https://doi.org/10.1103/PhysRevB.63.035401.
[55] A. Hjorth Larsen, J. Jørgen Mortensen, J. Blomqvist, I.E. Castelli, R. Christensen, M. Dułak, J. Friis, M.N. Groves, B. Hammer, C. Hargus, E.D. Hermes, P.C. Jennings, P. Bjerre Jensen, J. Kermode, J.R. Kitchin, E. Leonhard Kolsbjerg, J. Kubal, K. Kaasbjerg, S. Lysgaard, J. Bergmann Maronsson, T. Maxson, T. Olsen, L. Pastewka, A. Peterson, C. Rostgaard, J. Schiøtz, O. Schütt, M. Strange, K. S. Thygesen, T. Vegge, L. Vilhelmsen, M. Walter, Z. Zeng, K.W. Jacobsen, The atomic simulation environment-a Python library for working with atoms, J. Phys. Condens. Matter. Inst. Phys. J. 29 (2017) 273002, https://doi.org/10.1088/1361-648X/aa680e.
[56] B. Zhang, C.M. Ghimbeu, C. Laberty, C. Vix-Guterl, J.-M. Tarascon, Correlation between microstructure and Na storage behavior in hard carbon, Adv. Energy. Mater. 6 (2016) 1501588, https://doi.org/10.1002/aenm.201501588.
[57] E. Buiel, A.E. George, J.R. Dahn, On the reduction of lithium insertion capacity in hard-carbon anode materials with increasing heat-treatment temperature, J. Electrochem. Soc. 145 (1998) 2252, https://doi.org/10.1149/1.1838629.
[58] L. Sun, J. Li, L. Wang, E. Li, W. Huang, High temperature induced abundant closed nanopores for hard carbon as high-performance sodium-ion batteries anodes, J. Power Sources 624 (2024) 235474, https://doi.org/10.1016/j.jpowsour.2024.235474.
[59] Y. Liu, J.S. Xue, T. Zheng, J.R. Dahn, Mechanism of lithium insertion in hard carbons prepared by pyrolysis of epoxy resins, Carbon N Y 34 (1996) 193–200, https://doi.org/10.1016/0008-6223(96)00177-7.
[60] A. Beda, J.-M. Le Meins, P.-L. Taberna, P. Simon, C. Ghimbeu, Impact of biomass inorganic impurities on hard carbon properties and performance in Na-ion batteries, Sustain. Mater. Technol. 26 (2020) e00227, https://doi.org/10.1016/j.susmat.2020.e00227.
[61] K. Yu, H. Zhao, X. Wang, M. Zhang, R. Dong, Y. Li, Y. Bai, H. Xu, C. Wu, Hyperaccumulation route to Ca-rich hard carbon materials with cation self-incorporation and interlayer spacing optimization for high-performance sodium-ion batteries, ACS. Appl. Mater. Interfaces 12 (2020) 10544–10553, https://doi.org/10.1021/acsami.9b22745.
[62] H. Moon, M. Zarrabeitia, E. Frank, O. Böse, M. Enterría, D. Saurel, I. Hasa, S. Passerini, Assessing the reactivity of hard carbon anodes: linking material properties with electrochemical response upon sodium- and lithium-ion storage, Batter. Supercaps 4 (2021) 960–977, https://doi.org/10.1002/batt.202000322.
[63] H. Moon, A. Innocenti, H. Liu, H. Zhang, M. Weil, M. Zarrabeitia, S. Passerini, Bio-waste-derived hard carbon anodes through a sustainable and cost-effective synthesis process for sodium-ion batteries, ChemSusChem 16 (2023) e202201713, https://doi.org/10.1002/cssc.202201713.
[64] C. Matei Ghimbeu, A. Beda, B. Réty, H. El Marouazi, A. Vizintin, B. Tratnik, L. Simonin, J. Michel, J. Abou-Rjeily, R. Dominko, Review: insights on hard carbon materials for sodium-ion batteries (SIBs): synthesis – Properties – Performance relationships, Adv. Energy Mater. 14 (2024) 2303833, https://doi.org/10.1002/aenm.202303833.
[65] W. Luo, C. Bommier, Z. Jian, X. Li, R. Carter, S. Vail, Y. Lu, J.-J. Lee, X. Ji, Low-surface-area hard carbon anode for Na-ion batteries via graphene oxide as a dehydration agent, ACS. Appl. Mater. Interfaces 7 (2015) 2626–2631, https://doi.org/10.1021/am507679x.
[66] A. Beda, C. Vaulot, F. Rabuel, M. Morcrette, C.M. Ghimbeu, The role of specific and active surface areas in optimizing hard carbon irreversible capacity loss in sodium ion batteries, Energy. Adv. 1 (2022) 185–190, https://doi.org/10.1039/D2YA00004K.
[67] X. Tan, Q. Wen, L. Zhong, D. Lu, C. Wu, X. Wu, S.C. Smith, S. Chou, L. Kou, Critical role of potential-driven charge effects in hard carbon anodes for sodium storage, Angew. Chem. Int. Ed. 64 (2025) e202512830, https://doi.org/10.1002/anie.202512830.
[68] S.-J. Kinkelin, F. Röder, K. Vogel, M. Steimecke, M. Bron, A fundamental study on cyclic voltammetry at porous carbon thin-film electrodes, Electrochim. Acta 488 (2024) 144183, https://doi.org/10.1016/j.electacta.2024.144183.
[69] S. Fleischmann, J.B. Mitchell, R. Wang, C. Zhan, D. Jiang, V. Presser, V. Augustyn, Pseudocapacitance: from fundamental understanding to high power energy storage materials, Chem. Rev. 120 (2020) 6738–6782, https://doi.org/10.1021/acs.chemrev.0c00170.
[70] B.E. Conway, V. Birss, J. Wojtowicz, The role and utilization of pseudocapacitance for energy storage by supercapacitors, J. Power. Sources 66 (1997) 1–14, https://doi.org/10.1016/S0378-7753(96)02474-3.
[71] S.-J. Kinkelin, F. Röder, K. Vogel, M. Steimecke, M. Bron, A fundamental study on cyclic voltammetry at porous carbon thin-film electrodes, Electrochim. Acta 488 (2024) 144183, https://doi.org/10.1016/j.electacta.2024.144183.
[72] J.S. Weaving, A. Lim, J. Millichamp, T.P. Neville, D. Ledwoch, E. Kendrick, P. F. McMillan, P.R. Shearing, C.A. Howard, D.J.L. Brett, Elucidating the sodiation mechanism in hard carbon by Operando Raman spectroscopy, ACS. Appl. Energy. Mater. 3 (2020) 7474–7484, https://doi.org/10.1021/acsaem.0c00867.
[73] S. Pisana, M. Lazzeri, C. Casiraghi, K.S. Novoselov, A.K. Geim, A.C. Ferrari, F. Mauri, Breakdown of the adiabatic Born–Oppenheimer approximation in graphene, Nat. Mater. 6 (2007) 198–201, https://doi.org/10.1038/nmat1846.
[74] C.A. Howard, M.P.M. Dean, F. Withers, Phonons in potassium-doped graphene: the effects of electron-phonon interactions, dimensionality, and adatom ordering, Phys. Rev. B 84 (2011) 241404, https://doi.org/10.1103/PhysRevB.84.241404.
[75] Q. Chen, Q. Wen, C. Li, C. Li, P. Zhao, L. Li, X. Tan, J. Wang, X. Fan, S.-L. Chou, X. Wu, High-compaction spherical carbon with tunable rich pore structures for efficient sodium storage, Adv. Mater. 38 (2026) e15495, https://doi.org/10.1002/adma.202515495.
[76] X. Chen, J. Tian, P. Li, Y. Fang, Y. Fang, X. Liang, J. Feng, J. Dong, X. Ai, H. Yang, Y. Cao, An overall understanding of sodium storage behaviors in hard carbons by an "adsorption-intercalation/filling" hybrid mechanism, Adv. Energy. Mater. 12 (2022) 2200886, https://doi.org/10.1002/aenm.202200886.
[77] B. Manoj, A.G. Kunjomana, Study of stacking structure of amorphous carbon by X-ray diffraction technique, Int. J. Electrochem. Sci. 7 (2012) 3127–3134, https://doi.org/10.1016/S1452-3981(23)13940-X.
[78] S.-M. Lee, S.-H. Lee, J.-S. Roh, Analysis of activation process of carbon black based on structural parameters obtained by XRD Analysis, Crystals 11 (2021) 153, https://doi.org/10.3390/cryst11020153.
[79] L. Lu, V. Sahajwalla, C. Kong, D. Harris, Quantitative X-ray diffraction analysis and its application to various coals, Carbon N. Y 39 (2001) 1821–1833, https://doi.org/10.1016/S0008-6223(00)00318-3.
[80] C. Li, Q. Chen, Y. Zhang, P. Zhao, X. He, Q. Gu, J. Wang, S.-L. Chou, X. Wu, Molecular reconfiguration of pitch-derived hard carbon anodes with balanced thermodynamic stability and rapid sodium storage kinetics for high-performance sodium-ion batteries, Energy. Stor. Mater. 82 (2025) 104580, https://doi.org/10.1016/j.ensm.2025.104580.